HAL open science

Cyclic response of electrodeposited copper films. Experiments and elastic–viscoplastic mean-field modeling

Gautier Girard, Karol Frydrych, Katarzyna Kowalczyk-Gajewska, Marion Martiny, Sébastien Mercier

To cite this version:

Gautier Girard, Karol Frydrych, Katarzyna Kowalczyk-Gajewska, Marion Martiny, Sébastien Mercier. Cyclic response of electrodeposited copper films. Experiments and elastic–viscoplastic mean-field modeling. Mechanics of Materials, 2021, 153, pp.103685. 10.1016/j.mechmat.2020.103685 . hal-03051594

HAL Id: hal-03051594

https://hal.univ-lorraine.fr/hal-03051594v1

Submitted on 13 Feb 2021

HAL is a multi-disciplinary open access archive for the deposit and dissemination of scientific research documents, whether they are published or not. The documents may come from teaching and research institutions in France or abroad, or from public or private research centers.

L'archive ouverte pluridisciplinaire **HAL**, est destinée au dépôt et à la diffusion de documents scientifiques de niveau recherche, publiés ou non, émanant des établissements d'enseignement et de recherche français ou étrangers, des laboratoires publics ou privés.

Distributed under a Creative Commons Attribution - NonCommercial - NoDerivatives 4.0 International License

Cyclic response of electrodeposited copper films. Experiments and elastic-viscoplastic mean-field modeling.

G. Girard[a], K. Frydrych[b], K. Kowalczyk-Gajewska[b], M. Martiny[a] and S. Mercier[a] *

[a] Université de Lorraine -CNRS - Arts et Métiers ParisTech, Laboratoire d'Etude des Microstructures et de Mécanique des Matériaux, 7 rue Felix Savart, 57070 METZ - FRANCE

[b] Institute of Fundamental Technological Research, Polish Academy of Sciences, Pawińskiego 5B, 02-106 Warsaw, Poland

Abstract

The goal of the present work is to identify and model the elastic-viscoplastic behavior of electrodeposited copper films under tension-compression loadings. From the experimental point of view, as proposed in the literature, a film of copper is electrodeposited on both sides of an elastic compliant substrate. The overall specimen is next subjected to tensile loading-unloadings. As the substrate remains elastic, the elastic-plastic response of copper under cyclic loading is experimentally determined. A clear kinematic hardening behavior is captured. To model the mechanical response, a new elastic-viscoplastic self-consistent scheme for polycrystalline materials is proposed. The core of the model is the tangent additive interaction law proposed in (Molinari, 2002). The behavior of the single grain is rate dependent where kinematic hardening is accounted for in the model at the level of the slip system. The model parameters are optimized via an evolutionary algorithm by comparing the predictions to the experimental cyclic response. As a result, the overall response is predicted. In addition, the heterogeneity in plastic strain activity is estimated by the model during cyclic loading.

Keywords: electrodeposited copper, self-consistent scheme, elasto-viscoplasticity, kinematic hardening, experiments

This is a post-peer-review, pre-copyedit version of an article published in Mechanics of Materials. The final authenticated version is available online at: https://doi.org/10.1016/j.mechmat.2020.103685.

1 Introduction

The mechanical behavior of polycrystalline FCC metals, and copper in particular, is constantly addressed in the literature. To quantify the mechanical fields in a polycrystal, crystal plasticity finite element calculations on aggregates (e.g. Farooq et al. (2020)) or mean field approaches based on self-consistent scheme (see for instance

*Corresponding author, e-mail: sebastien.mercier@univ-lorraine.fr

Zecevic et al. (2017)) are the two main options. Both models have to be calibrated by comparisons with precise material characterizations including macroscopic tests and microstructural observations.

The present research is driven by the needs of reliability of Printed Circuit Boards (PCB) requested especially for aeronautic, space or automotive applications. A PCB is a layered material containing mostly woven composites, copper but also active or passive components embedded in its core to achieve a higher interconnection density. In PCB, different kinds of copper are present. First of all, the conducting traces, usually laminated on a woven composite, are made of copper (rolled annealed or electrodeposited, thickness in the range 10 to 70 μm). In addition, holes, drilled through the PCB thickness, are coated by electrodeposited copper produced by the PCB manufacturers. These coated holes are named Plated Through Holes (PTH). They ensure the electrical connection between the interconnected traces on each layer. Due to thermal cycling and mismatch in the coefficients of thermal expansion, copper will experience plasticity during thermal cycling of a PCB, leading to low cycle fatigue.

The reliability of PTHs by means of finite element simulations has been addressed widely in the literature, see for instance Fu et al. (1998), Fellner et al. (2016), Salahouelhadj et al. (2014), Watanabe et al. (2018). A critical point in such simulations is the right reconstruction of the mechanical behavior of copper, especially under cyclic loading. However, in most of the cited studies copper behavior is identified from a monotonic or loading/unloading tensile tests. If kinematic hardening is accounted for, like in Fu et al. (1998), the behavior is representative of an oxygen free high conductivity (OFHC) wrought copper, which probably has a behavior differing from copper films used in PCBs.

There exists a huge literature dedicated to the mechanical response of bulk pure copper with a focus made on cyclic loading and associated microstructural changes, see for instance Mughrabi (1978), Rasmussen and Pedersen (1980) among others. Less mechanical tests have been proposed to determine the cyclic response of copper film in the presence of plasticity. Compression loading cannot be imposed to a copper film due to buckling. Therefore, the prescribed method is to deposit the copper film on a compliant substrate. Macionczyk and Brückner (1999) used this method to determine the cyclic behavior of an AlCu film from the overall force-displacement measurement. The elastic behavior of the substrate was identified by an independent mechanical test. Thus from the overall and substrate responses, the authors were able to define the stress-strain response of the copper alone, nevertheless neglecting the transversal stress induced in the film due to the mismatch in Poisson's ratio between the substrate and the copper film. One can also refer to Mönig et al. (2004), Kraft et al. (2001) or Fellner et al. (2014) for similar experiments and copper characterization. It has been also observed that microstructural features influence the mechanical response of copper film. Film thickness, thermal treatments or grain size, shape and orientations, manufacturing process generate different copper mechanical behaviors, as pointed out experimentally by Schwaiger et al. (2003) or Wimmer et al. (2014) for PCB applications or by Adzima et al. (2017) for forming process of copper thin sheet.

To account for all expected dependencies on microstructural features, elastic-viscoplastic multiscale approaches for polycrystalline materials were proposed in the literature, usually as counterparts of formulations developed earlier for composite materials. For example, in Liu et al. (2003) an incremental variational approach (Ponte Castañeda and Suquet (1998)) is used, while in Lebensohn et al. (2012) full field simulations of elastic-viscoplastic polycrystalline copper are performed employing Fast Fourier Transform technique (Moulinec and Suquet (1998)). Another category is a set of mean-field models based on interaction law or localization rule. The works of the latter category will be discussed in more detail since they are more closely related to the approach followed in the present study.

The contributions dealing with the micromechanical schemes applicable to the elastic-viscoplastic polycrystalline materials can be classified into five groups, namely

1. analyses employing simple *iso-strain Taylor-Lin model* but set in the large strain framework (Asaro and Needleman (1985)). Using such model the texture evolution in polycrystalline copper under cyclic loading was predicted e.g. by Tóth et al. (2000) or Bacroix et al. (2018);

To overcome the weakness related to the assumption of uniform strain the approaches based on the classical Eshelby result and a general concept of the self-consistent scale transition scheme have been next considered. Note that because of the simultaneous presence of both elastic and viscous properties of grains and an implicit character of the self-consistent interaction relation, assessment of overall behavior using such an approach is still a challenge. Basically four settings addressing this issue can be found, i.e.:

2. use of *the Laplace-type transform technique*, following early work of Hashin (1966). However, extensions of this rigorous formalism to polycrystals, where elasticity is accompanied by non-linear viscous properties, lead to rather complex formulations (Masson and Zaoui (1999));

3. use of *projection operator and translated fields* of Sabar et al. (2002). In this setting Mareau and Berbenni (2015) proposed to linearize the non-linear viscous response in a tangent way (Molinari et al. (1987)) to model the response of polycrystalline metals via a self-consistent scheme and compared the predictions to FFT results;

4. formulations based on *the additive tangent interaction rule* (Molinari et al. (1997), Molinari (2002)). Abdul-Latif et al. (2018) adopted this interaction law, although simplified by use of the isotropic Hill tensors, to simulate ultrafine grained polycrystalline and nanocrystalline copper. A finite strain version of the additive law combined with a self-consistent scheme was developed by Wang et al. (2010a). Recently, Zecevic and Lebensohn (2020) developed a non-incremental self-consistent scheme for elastic-viscoplastic materials based on the additive tangent interaction rule;

5. related to the previous one but conceptually different *the approach of sequential linearization* (Kowalczyk-Gajewska and Petryk (2011)). For the Mori-Tanaka scheme, the method coincides with the additive tangent approach as developed in Mercier and Molinari (2009). For the self-consistent scheme used for polycrystals an additional accommodation step was added to obtain more satisfactory predictions. Preliminary results of such approach for polycrystalline materials have been presented in Kowalczyk-Gajewska (2011) without comparison with experimental data.

The above models are able to capture the material response at the level of the RVE. To simulate the response of a structure under various loading conditions, mean-field models can be on the one hand embedded into a finite element (FE) software. Segurado et al. (2012) implemented the viscoplastic self-consistent (VPSC) scheme (Molinari et al. (1987), Lebensohn and Tomé (1993)) in a user-defined material UMAT subroutine. The authors validated the model using uniaxial tension and simple shear of a FCC AA6116 Al alloy. Texture evolutions were accurately predicted. Nevertheless, the elastic strain within each grain was not accessible. So recently, an elastic-plastic self-consistent (EPSC) scheme was implemented in a finite element software by Zecevic et al. (2017). In that case, the scale transition in each grain is carried out so the elastic strain development within individual grains is accessible. The integration of the EPSC equations was performed explicitly for each time increment. But an implicit FE software was used to carry out compression and cyclic loading on various alloys: AA6022 T4 aluminium alloy, DP590 steel and α-Ti. Note that kinematic hardening was accounted for to better describe cyclic loadings. Recently, Zecevic and Knezevic (2019) developed an implicit integration procedure of the EPSC model in ABAQUS

software. They considered cup drawing of an AA6022 T4 sheet. One can also mention the work of Msolli et al. (2016) who also coupled FE calculations and an elastic-viscoplastic mean field approach to simulate cup drawing. They considered the forming process of AISI 304L austenitic steel taking into account phase transformation. The tangent additive interaction law coupled with a Mori-Tanaka scheme was implemented in ABAQUS software.

On the other hand, full-field finite element simulations of polycrystals subjected to cyclic loading can also be found in the literature. For instance, Cruzado et al. (2018) modeled the elastic-plastic behavior of IN718 alloy under uniaxial cyclic deformation tests with fully reversed deformation $R_\varepsilon = -1$. They considered FE calculations of a RVE containing 300 grains. The crystal behavior was based on crystal plasticity model and kinematic hardening was introduced at the level of the slip system.

The aim of the present study is two-fold. Firstly, we would like to establish experimental and modeling tools enabling precise assessment of inelastic behavior of polycrystalline ED copper under cyclic loadings. For the modeling approach, as a relevant tool for polycrystalline materials, a multiscale micromechanical approach based on the self-consistent scheme is selected. Therefore, the second goal of the present study, is to extend the elastic-viscopastic self-consistent scheme developed for two-phase materials in Mercier and Molinari (2009) or Kowalczyk-Gajewska and Petryk (2011) to polycrystalline materials. To do so, the anisotropy of the tangent viscoplastic modulus is accounted for. Unlike in Wang et al. (2010a), the mathematical structure of the aggregate response is not predefined and is a natural outcome of the modeling. The proposition of a new self-consistent scheme for elastic-viscoplastic polycrystals is now possible after careful validation of all necessary steps in the course of previous studies. Indeed, in Mercier et al. (2005), the additive tangent interaction law of Molinari (2002) has been validated by considering the Eshelby problem. It was checked by the authors that the average mechanical fields within the inclusion domain predicted by the interaction law were in close agreement with the ones captured by finite element calculations. In the second step, Mori-Tanaka and self-consistent schemes for two-phase composite materials were proposed in Mercier and Molinari (2009) and revisited in Kowalczyk-Gajewska and Petryk (2011). The validation of the *Mori-Tanaka* scheme for two-phase elastic-viscoplastic materials with isotropic hardening was done by comparison with calculations on representative volume elements containing multiple inclusions during cyclic loadings, see Czarnota et al. (2015). Moreover it is clear that for cyclic loading, Bauschinger effect is present. Therefore a Mori-Tanaka scheme for two-phase materials with kinematic hardening was recently developed in Mercier et al. (2019) and compared well with finite element predictions. It was shown that the additive tangent interaction law is capable to manage kinematic hardening with good efficiency. Finally, the goal proposed in this work is to integrate all the validated stages in a new elastic-viscoplastic *self-consistent* scheme dedicated to polycrystals. As polycrystal films are of great interest in current applications (micro-electronics, mems...), while their responses are really sensitive to processing routes and thickness, we perform our own experimental characterization, so that all the inputs of the multi-scale approach are well defined. This enables validation of the proposed modeling framework.

The paper is organised as follows. First, tensile loading-unloading tests prescribed to a sample made of a compliant elastic substrate with two external layers of copper are described. We propose to extend the work of Macionczyk and Brückner (1999) by accounting for the transversal effect due to Poisson's ratio mismatch which induces biaxial stress in the copper film. The magnitude of the loading is chosen so as to trigger plasticity during cycles, situation which is encountered in a PCB during a thermal cycle. As a result, a combined kinematic and isotropic hardening is clearly observed for copper. In addition to the identification of the mechanical response, the texture has been measured to provide microstructural information. Next, in order to model the cyclic response of copper films, a self-consistent scheme based on the tangent additive interaction law of Molinari (2002) (see also

Kowalczyk-Gajewska and Petryk (2011)) is developed. The small strain assumption is followed. The mean field approach is able to reproduce with a good accuracy the cyclic response of electrodeposited copper considered in the present work. Additional outcomes of calculations such as plastic activities within grains are discussed.

2 Characterization of the elastic-plastic behavior of a copper film

In this section, the method used to apply tensile-compressive loadings in copper films via a compliant substrate is exposed. Some developments are presented which enable to determine the behavior of copper from the response of the substrate/copper assembly.

In a multi-layer PCB, various types of copper can be found. Copper foils found in each layer of the board can be of different origins. One can find electrodeposited, wrought or laminated copper types which have undergone different thermo-mechanical treatments, allowing them to be more or less capable of sustaining large deformation and sensitive to fatigue. These copper layers are available with thicknesses varying between 2 and 500 μm. In this work, an ED (electrodeposited) copper produced by a PCB manufacturer is selected. The film thickness is approximately 45 μm. The method proposed here is nonetheless applicable to any copper film used in a PCB or any metal foil.

2.1 Experimental setup and measurements

Figure 1b presents the adopted specimen where the substrate is coated with two copper layers present on both sides of the specimen for symmetry purpose. The specimen is designed in order to identify the plastic behavior of copper. For that purpose, during a tensile loading, the substrate must remain elastic while the copper undergoes plastic deformation. During unloading, the substrate will tend to recover its elastic strain and drive the copper in compression. By applying loading/unloading cycles, the copper is subjected to tension-compression cycles. The substrate used for this study is a laminate (often encountered in PCBs) composed of glass fibers and epoxy based matrix. The overall behavior of the substrate is orthotropic.

The method used to deposit ED copper on the substrate is a two-stage process. First, a pre-impregnated substrate is pressed with 2 μm thick copper films on both sides. The curing of the B-stage resin in the substrate ensures good adhesion properties of the interface. In a second step, ED copper is electrodeposited at room temperature on the copper surface to reach the desired film thickness (45 μm). Self-annealing of electrodeposited copper films has been shown to happen after deposition within tens of hours at room temperature (Ritzdorf et al. (1998), Okoro et al. (2010)). Therefore, one can assume that the sample is almost free of internal stresses a few hours after being processed. In the following, the assembly of ED copper layers with composite substrate will be designated as ED sample.

The test specimen is a multi-layer assembly (woven composite + ED copper). The proportions of each material must be carefully chosen. Indeed, it is necessary to have a substrate thick enough to induce compression in copper during unloading, while the thickness of copper must be significant so that its presence has a noticeable effect on the measured force. Our choice of a 200μm substrate and a 45 μm copper film on both sides proved to fulfill these requirements.

After pressing and curing, the substrate may have a thickness differing from the as-received material. The control of the thickness of electrodeposited copper is also crucial. Indeed, any variation on the measured thicknesses will have an influence on the evaluated stresses in both materials. Therefore, before testing, thicknesses of

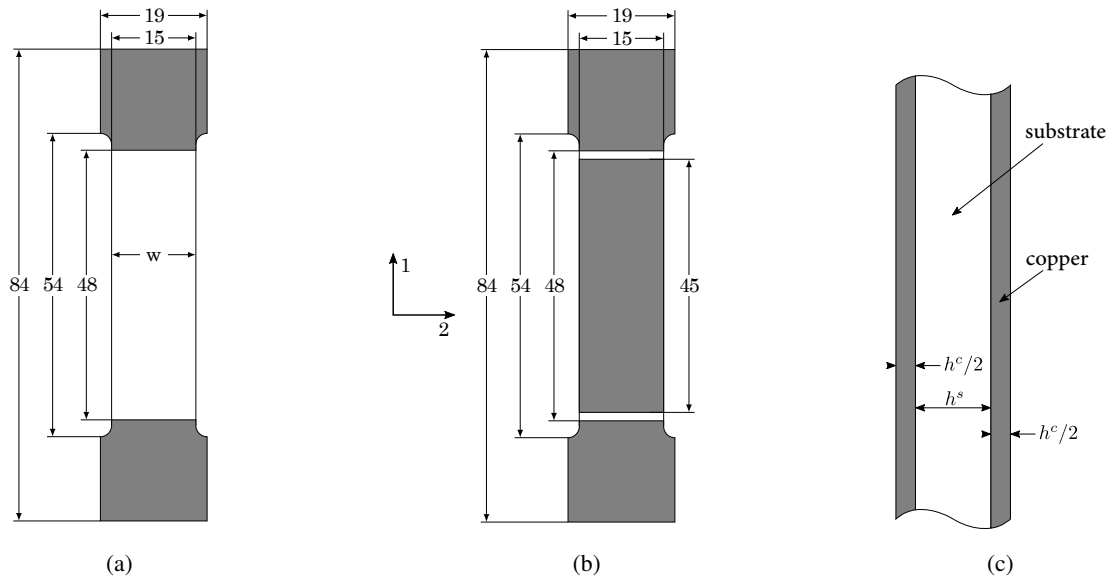

Figure 1: Layout of specimens used for the identification of (a) the elastic behavior of the substrate, (b) the elastic-plastic behavior of copper. The gauge length is made of substrate with layers of copper on both sides. (c) Side view of the specimen gauge section described in (b). h^s is the substrate thickness. The copper film thickness is $h^c/2$ leading to a total thickness of copper h^c in the sample. Dimensions of all geometrical features are in mm.

substrate and copper layers are measured by optical microscopy with the following method. Cross-section images of samples are analyzed. The substrate/copper interface observed on Figure 2a is relatively rough. This allows a good adhesion between the two materials, but leads to variations on the local thickness. On microsections, the copper appears much brighter than the substrate in Fig. 2a. As a consequence, the contrast in brightness of pixels along the cross-section is used to measure thicknesses. A dedicated Python program has been developed to detect positions where a rapid change in the brightness profile is observed. Measurements are repeated many times on each image and on several parts of the sample. One example of measurements made on a microsection is shown in Fig. 2b. The averaged thickness is finally computed from around 100000 individual measurements (dozens of images). Results are presented in Table 1.

Sample	ED sample amplitude 1		ED sample amplitude 2	
Material	substrate	copper	substrate	copper
	h^s	$h^c/2$	h^s	$h^c/2$
Mean thickness [μm]	174.1	44.8	174.1	46.0

Table 1: Mean thicknesses of the substrate and ED copper films, measured by optical microscopy. The standard deviation on the thickness measurements is 1.6 μm for the substrate and 1 μm for the copper layers.

In order to identify the substrate behavior, the copper present on both sides has been etched so that the gauge section of the sample is only made of the substrate material, as represented on Figure 1a. Samples with different orientations (0°, 45° and 90°) with respect to the warp direction of the woven laminate, are submitted to five

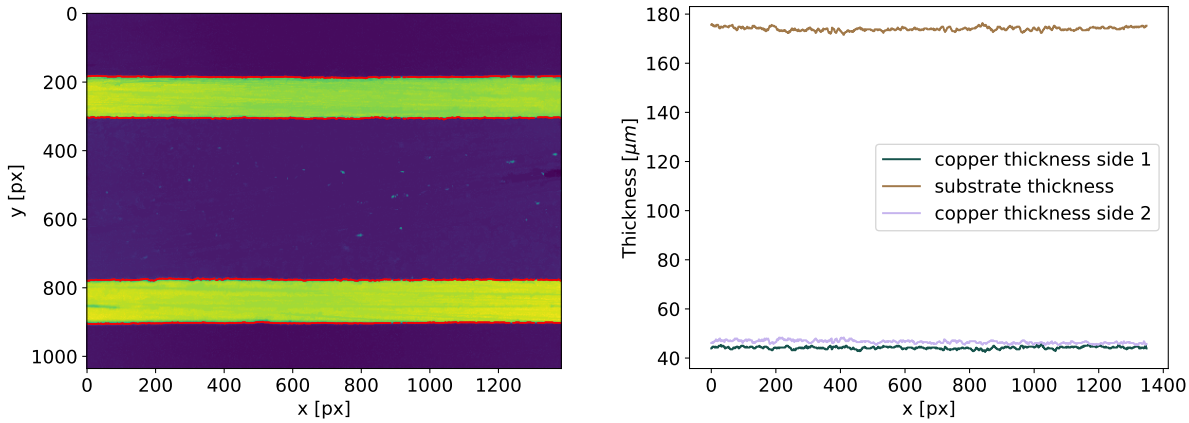

(a) (b)

Figure 2: (a) Microsection of ED sample with detected boundaries superimposed (red dots). (b) Thickness measurements made on the microsection. The mean thickness over several images is reported in Table 1.

cycles within the elastic domain to evaluate the in-plane elastic behavior. The tensile machine is an Instron E3000 equipped with a 1 kN load cell. Longitudinal and transversal strains have been captured by digital image correlation using VIC2D software. The measured elastic coefficients of the substrate are presented in Table 2.

E_1^s [GPa]	E_2^s [GPa]	ν_{12}^s [-]	G_{12}^s [GPa]
22.6	25.9	0.18	4.36

Table 2: In-plane elastic properties for the substrate, measured at room temperature.

Tests on ED samples (Figure 1b) have been conducted on the same tensile machine. The cross-head velocity is set to 2 mm/min. Figure 3 presents the overall force in the loading direction as a function of the macroscopic longitudinal strain for two selected cycles. Two limits in force are imposed during experiments: an upper limit so that the substrate remains in the elastic domain and a lower limit to avoid buckling. The longitudinal strain measured via digital image correlation corresponds to the average strain in the gauge section of the specimen, see Figure 1. ED samples have been tested at different force amplitudes: *amplitude 1* (named Ampl. 1) between 10 and 700 N and *amplitude 2* (named Ampl. 2) between 10 and 560 N. Each experiment for ED materials was repeated once with no significant difference observed.

The ED copper is not available as a freestanding foil, as it is produced via electrodeposition by the PCB manufacturer to cover the substrate. The elastic properties of ED copper are deduced from cycles on ED samples. It is assumed in this section that the response is isotropic, assumption consistent with the texture measurements presented later in Fig. 5. From the analysis of the unloading stages in all cycles, the measured longitudinal and transversal strains in the elastic regime, the measurement of the thicknesses (see Table 1) and the elastic behavior of the substrate (see Table 2), the Young's modulus and Poisson's ratio are determined: $E_{ED} = 80$GPa and $\nu_{ED} = 0.33$.

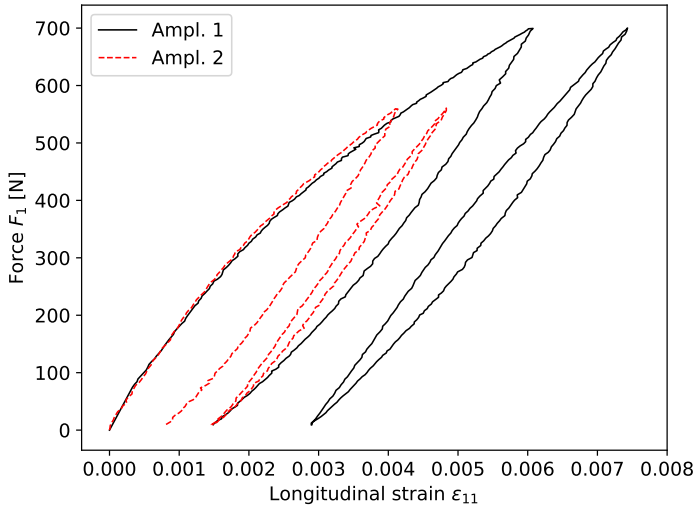

Figure 3: Force versus longitudinal strain for ED sample. Only the first and 50th cycles are displayed. Geometrical features of the sample are presented in Table 1.

2.2 Determination of the elastic-plastic behavior of copper

In the previous section, multi-layer samples were loaded/unloaded, see Figure 3. From the knowledge of the substrate behavior, the stress-strain response of copper is captured. More details can be found in Appendix A. Note that from DIC measurements on the free surface of the sample, the shear component ε_{12} has been measured together with the longitudinal and transversal strains and is seen to be of limited amplitude (around two orders of magnitude smaller than the two remaining in-plane components) during the whole loading.

Figure 4 presents the evolution of σ^c_{11} and σ^c_{22} for the ED copper during 50 cycles for both loading conditions: Ampl. 1 and Ampl. 2. For the Ampl. 1 amplitude, the stress component σ^c_{11} (resp. σ^c_{22}) reaches a maximum value of 240 MPa (resp. 40 MPa). It is observed that σ^c_{22} remains limited; its maximum value corresponding to approximately 17 $\%$ of σ^c_{11}. As Ampl. 2 presents a limited maximum force, strains are smaller. The loop at stabilized cycle is less marked. One observes in Fig. 4 that the longitudinal stress level during first tensile loading stage is slightly different for the two tests (3 $\%$ higher for Ampl. 2 condition). Such a limited difference was already observed in Fig. 3. The origin of the difference comes mainly from the process of electrodeposition. Two specimens have barely exactly the same mechanical behavior. From Fig. 4, copper materials present a clear kinematic hardening during cycles. After 50 cycles, the stress-strain response exhibits still a loop. This observation is better illustrated in Fig. 10. The cycle is wider for Ampl. 1. From this observation, we will adopt next Ampl. 1 for the calibration of the multi-scale model parameters.

2.3 Microstructure observations

The texture of ED copper has been analyzed by X-ray diffraction (XRD) with an azimuth step of 5°, an inclination step of 2.5^{o} and a linear displacement of the sample of 3 mm during the measurement. The X-ray beam has an interaction zone of approximately 1 mm^2, with a depth of approximately 10 μm. The orientation density functions have been computed from the texture measurements by the software ATEX from Beausir and Fundenberger (2017). The stereographic projections are presented in Figure 5. The X direction represented on these figures corresponds

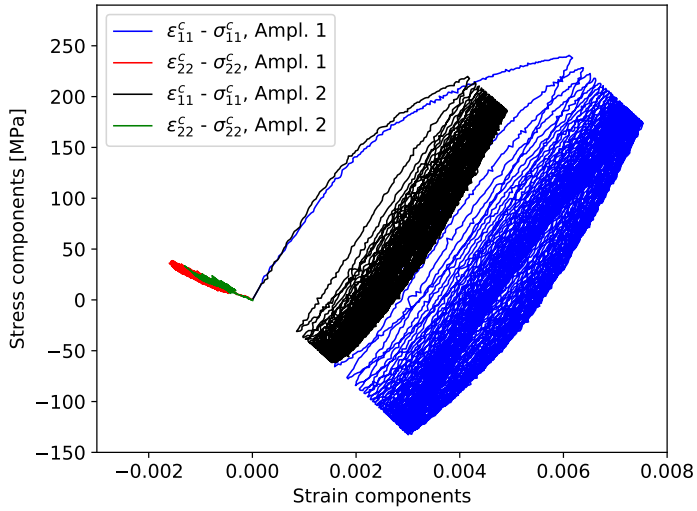

Figure 4: Stress-strain response of ED copper during cycles for amplitude Ampl. 1 (force between $10N$ and $700N$, blue and red curves) and for Ampl. 2 (force between $10N$ and $560N$, black and green curves). The evolution of components in the longitudinal and the transverse directions are presented. The curves are extracted from the response of substrate + copper presented in Figure 3.

to the tensile direction, see Fig. 1. ED copper has a weak texture with a symmetry close to cylindrical. There is no preferred orientation in the plane, but there is a slightly preferred orientation along the out-of-plane direction, namely (111) crystal planes are parallel to the normal of the plane (z-axis). The process of electrodeposition is also supposed to provide such planar isotropy, close to isotropy.

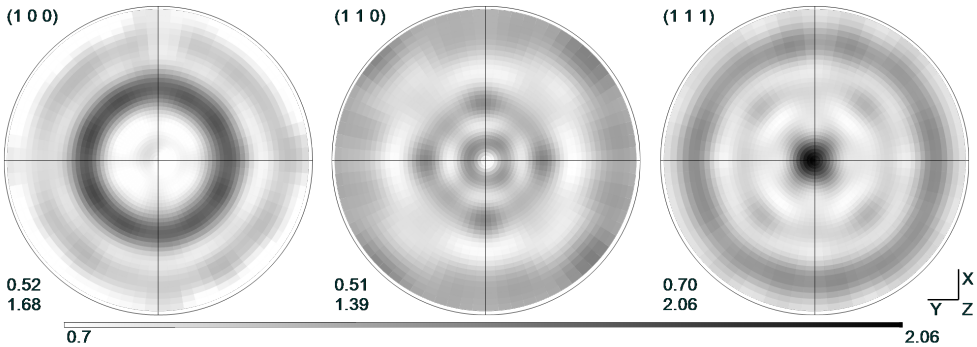

Figure 5: Pole figures measured by X-ray diffraction on electrodeposited (ED) copper.

The microstructure of ED copper has also been analyzed using Scanning Electron Microscope and EBSD (Electron Backscatter Diffraction) detector. EBSD measurements have also confirmed the planar isotropy of orientations. From the EBSD band contrast map, the grain size and the presence of annealing twins are captured, see Fig. 6.

Boundaries of grains in black or of annealing twins in red color are highlighted in Figure 6. The annealing twin boundaries accumulate dislocations during deformation so that they can loose their twin boundary character and

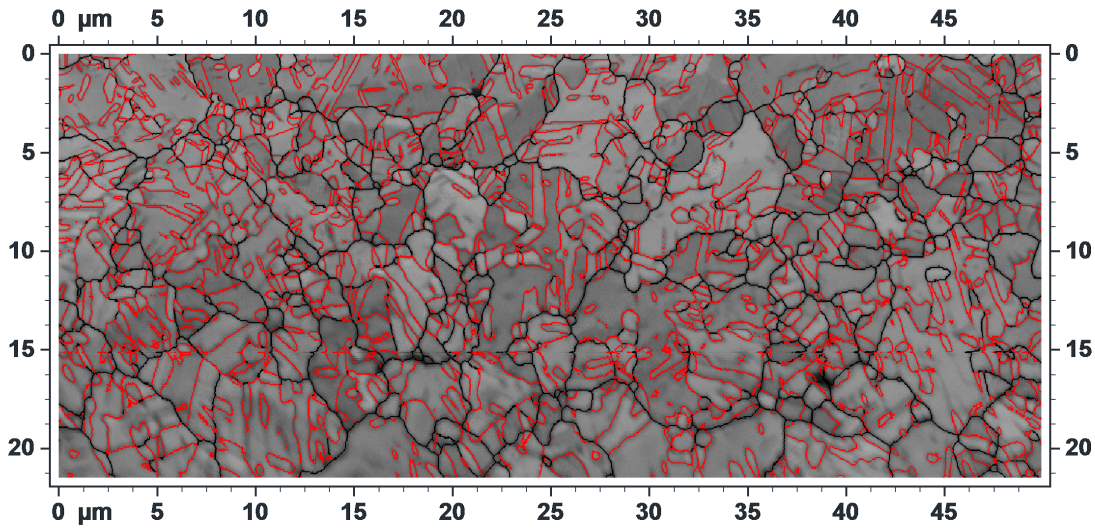

Figure 6: EBSD band contrast map of the microstructure. The grain boundaries are drawn in black (disorientation above 5°) and the twin boundaries are drawn in red (disorientation between 58° and 62°).

transform into general boundaries, see for instance Bozzolo and Bernacki (2020) for more details about annealing twins. From TEM observations, Wang et al. (2010b) concluded that the movement of non-coherent segments can occur under an applied external stress field as long as they have not lost their twin character as a result of dislocation accumulation, but only over very short distances (few tens of nm). Moreover, since deformation is carried out at room temperature, their thermally-activated migration during deformation is also very unlikely. Therefore, in our work, twins will be mechanically treated as grains.

From EBSD measurements (Fig. 6), the surface of each grain has been measured by counting the number of pixels contained in each grain, where a grain is defined as a group of neighboring pixels with a disorientation smaller than 5°. In our experiment, the pixel size is 0.03 μm x 0.03 μm. Note that grains composed of 4 pixels or less have not been considered. Therefore, the number of grains is $N_g = 1626$. We observe that the number of grains with an area larger than $2(\mu m)^2$ is limited (122 grains among 1626 grains). 1384 grains have an area smaller than $1(\mu m)^2$. From the measurement, a number frequency grain size distribution is defined in Fig. 7a. For each grain i (see Fig. 6), the number of pixels composing the grain and the corresponding surface a_i are captured. From the Equivalent Circle Area method (EqCA), the grain size $d^i_{EqCA} = \sqrt{\frac{4a_i}{\pi}}$ is obtained. The number-weighted mean grain size $\bar{D}_N$ is defined as:

$$\bar{D}_N = \frac{1}{N_g}\sum_{i=1}^{N_g} d^i_{EqCA}. \tag{1}$$

The corresponding mean grain size (or diameter) is $\bar{D}_N = 0.65\mu m$. The experimental density function has been fitted by adopting a log-normal probability density function (pdf):

$$f(d) = \frac{1}{d\sigma\sqrt{2\pi}}\exp(-\frac{(\ln(d)-\mu)^2)}{2\sigma^2}), \tag{2}$$

where μ and σ are the mean value and the standard deviation of $\ln(d)$. The corresponding values of these two parameters for the log normal pdf presented in Fig. 7a are $\mu = -0.805$ and $\sigma = 0.880$.

Note that the experimental area-weighted grain size distribution has also been evaluated in Fig. 7b leading to an area-weighted mean grain size:

$$\bar{D}_A = \frac{1}{\sum_{i=1}^{N_g} a_i} \sum_{i=1}^{N_g} a_i d^i_{EqCA}. \tag{3}$$

For our material, one gets: $\bar{D}_A = 2.16\mu m$. The parabola curves presented in Fig. 7b correspond to a constant number of grains in the bin, Tóth et al. (2013). For instance, only 7 grains have a grain size larger than $4\mu m$.

Several evaluations of the mean grain size $\bar{D}_N$ and $\bar{D}_A$ have been conducted by considering grains with surface larger than 2 pixels, 3 pixels, 5 pixels and 8 pixels. From the additional calculations, it has been found that D_N is varying from $0.599\mu m$ to $0.686\mu m$. The effect on the area-weighted grain size $\bar{D}_A$ is limited (variation smaller than 0.1%). Therefore, one still has $\bar{D}_A = 2.16\mu m$.

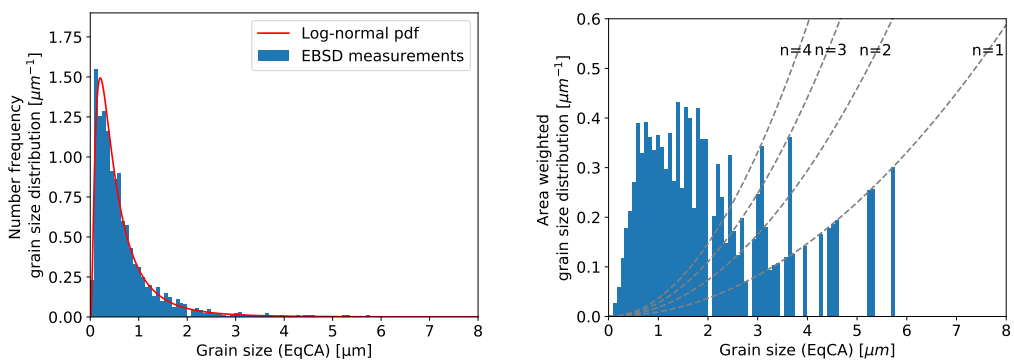

(a) (b)

Figure 7: Density function of (a) number-weighted grain size frequency, (b) area-weighted grain size frequency. The pixel size of the EBSD measurement is 0.03 μm. Grains with area of 4 pixels or less have been disregarded. The width of the bins in the histogram plot is 0.08 μm. The parabola curves presented in Fig. 7b correspond to a constant number of grains in the bin.

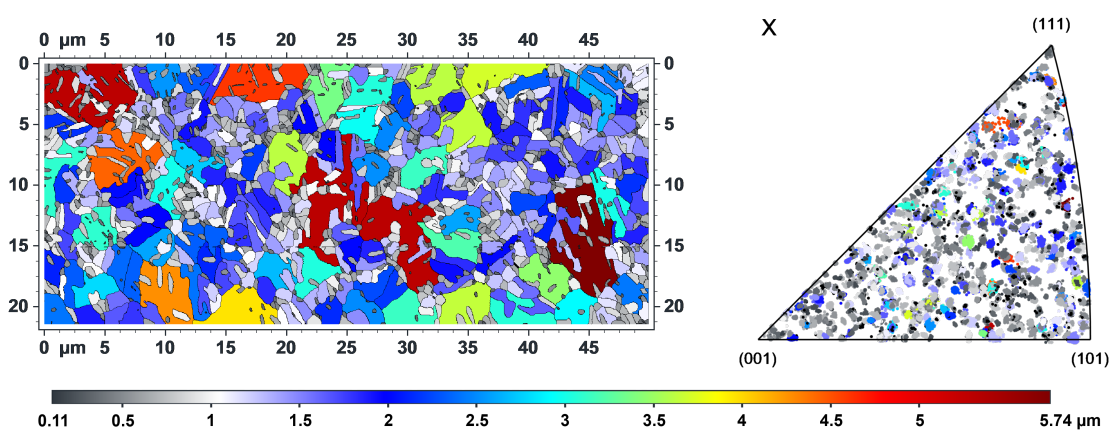

Figure 8: Color map of area, related grain size and associated inverse pole figure of grain size. The position of a respective point in this inverse pole figure provides the orientation of the tensile axis (*i.e.* x axis) with respect to the local axes of each grain.

To clarify the distribution of grain size and related orientations, each grain of the EBSD map presented in Fig. 6 is colored on Fig. 8 according to its size, and the inverse pole figure relative to the tensile axis is plotted with the same color coding. Figure 8 shows that there is no correlation between the grain size and their orientation. In other words, grains have random orientations (points covering the whole inverse pole figure), regardless of their size (color).

In our work, with the observed mean grain size ($\bar{D}_N$ or $\bar{D}_A$), the number of grains in one copper layer of 45 μm thickness is quite large (approximately 60 adopting $\bar{D}_N$ or approximately 20 adopting $\bar{D}_A$). This finding has been confirmed by a FIB-SEM observation along the through-thickness of the copper film (results not presented here). By adopting a line intercept method, the number of intersection points with boundaries counted along the thickness is larger than 20. For thin film, surface effect, constraint due to a substrate or role of the number of grains within the thickness have been investigated by Crystal Plasticity Finite Element Method (CPFEM). With such time consuming calculations, the number of grains considered is usually limited (from 10 to hundreds of grains). Buchheit et al. (1997) showed that specimens with approximately five grains in the thickness have a macroscopic response which is consistent with continuum polycrystalline behavior (where surface constraints may be neglected). Keller and Hug (2017) confirmed these results by considering FE calculations and experiments on Nickel films. The surface effect can be negligible for a critical ratio (thickness over grain size) of around five to ten. In their introduction, they mentioned that this ratio can vary from three to twenty. Siska et al. (2007) considered CPFEM of a columnar film (with only one grain in the thickness). They clearly evidenced the role of surface effect and the substrate on the roughness during deformation. Haldrup et al. (2009) considered a representative volume element with 100 grains subjected to tensile loading, adopting periodic boundary conditions (representative of bulk material) or free (representative of surface) boundaries. They concluded that for OFHC copper, boundary conditions have an effect on the response, but do not lead to a complete change of behavior. Note that for their aggregate, only 5 to 6 grains were present in the thickness. As a consequence, even if the film is quite thin in our work, it is reasonable to consider the present ED copper as a polycrystal, where surface and substrate effects may be ignored in a first approximation. In the future, it could be of interest to develop CPFEM calculations on representative volume elements generated from real 3D microstructures obtained from FIB-SEM to validate this assumption. Next, we propose to adopt an elastic-viscoplastic mean field approach for modeling the response of ED copper.

3 Multiscale modeling of elastic-viscoplastic polycrystalline aggregate

3.1 Constitutive relation for the single crystal

In this section, the constitutive equations describing the elastic-viscoplastic behavior of a single crystal are formulated. A small strain theory is adopted. The total strain rate $\dot{\boldsymbol{\varepsilon}}_g$ in the grain g is the sum of an elastic $\dot{\boldsymbol{\varepsilon}}_g^{\mathrm{e}}$ and a viscous strain rate $\dot{\boldsymbol{\varepsilon}}_g^{\mathrm{v}}$:

$$\dot{\boldsymbol{\varepsilon}}_g = \dot{\boldsymbol{\varepsilon}}_g^{\mathrm{e}} + \dot{\boldsymbol{\varepsilon}}_g^{\mathrm{v}}. \tag{4}$$

The elastic constitutive equation for the crystal is given by the linear anisotropic Hooke's law:

$$\dot{\boldsymbol{\sigma}}_g = \mathbf{A}_g^{\mathrm{e}} \cdot \dot{\boldsymbol{\varepsilon}}_g^{\mathrm{e}} \quad \text{or} \quad \dot{\boldsymbol{\varepsilon}}_g^{\mathrm{e}} = \mathbf{M}_g^{\mathrm{e}} \cdot \dot{\boldsymbol{\sigma}}_g \,, \tag{5}$$

where $\mathbf{A}_g^{\mathrm{e}}$ is the fourth order elastic stiffness tensor. The associated compliance tensor is $\mathbf{M}_g^{\mathrm{e}} = (\mathbf{A}_g^{\mathrm{e}})^{-1}$.

The plastic deformation inside the grain is due to slip. The rate-dependent crystal plasticity formulation is used for a constitutive description at the level of the single grain, see Pan and Rice (1983) or Asaro and Needleman (1985). The plastic strain rate tensor inside the grain is due to all activities at the level of each slip system:

$$\dot{\boldsymbol{\varepsilon}}_g^{\mathrm{v}} = \sum_{r=1}^{N} \dot{\gamma}^{r,g} \mathbf{P}^{r,g}\,, \quad \text{where} \quad \mathbf{P}^{r,g} = \frac{1}{2}(\mathbf{m}^{r,g} \otimes \mathbf{n}^{r,g} + \mathbf{n}^{r,g} \otimes \mathbf{m}^{r,g}), \tag{6}$$

where vectors $\{\mathbf{m}^{r,g}, \mathbf{n}^{r,g}\}$ denote the slip direction and the slip plane unit normal for the slip system r in the grain g, respectively. $\dot{\gamma}^{r,g}$ is the slip rate, $\otimes$ the tensorial product and $\mathbf{P}^{r,g}$ the orientation tensor. The resolved shear stress is defined as:

$$\tau^{r,g} = \mathbf{P}^{r,g} : \boldsymbol{\sigma}_g, \tag{7}$$

where : denotes the double contracted product.

The relation between the slip rate and the resolved shear stress at the level of the slip system follows the rate-dependent power law with isotropic and kinematic hardening developed in Hennessey et al. (2017):

$$\dot{\gamma}^{r,g} = \dot{\gamma}_0 \left| \frac{\tau^{r,g} - \chi^{r,g}}{\tau_{\mathrm{c}}^{r,g}} \right|^n \mathrm{sign}(\tau^{r,g} - \chi^{r,g})\,, \tag{8}$$

in which $\chi^{r,g}$ and $\tau_{\mathrm{c}}^{r,g}$ are the slip system backstress (scalar value) and the critical resolved shear stress for the slip system r in the grain g, correspondingly. Scalar parameter $\dot{\gamma}_0$ is a reference slip rate and n is the inverse of the strain rate sensitivity. The tangent viscous compliance tensor for the power law (8),

$$\mathbf{M}_g^{\mathrm{v}} = \frac{\partial \dot{\boldsymbol{\varepsilon}}_g^{\mathrm{v}}}{\partial \boldsymbol{\sigma}_g} \tag{9}$$

is given by the following formula :

$$\mathbf{M}_g^{\mathrm{v}} = n\dot{\gamma}_0 \sum_{r=1}^{N} \left| \frac{\tau^{r,g} - \chi^{r,g}}{\tau_{\mathrm{c}}^{r,g}} \right|^{n-1} \frac{\mathrm{sign}(\tau^{r,g} - \chi^{r,g})}{\tau_{\mathrm{c}}^{r,g}} \mathbf{P}^{r,g} \otimes \mathbf{P}^{r,g}\,. \tag{10}$$

By the definition of the tangent compliance tensor, the slip system backstress has been treated as an internal variable independent of the stress state, similarly to the recent development of the additive interaction law combined with the Mori-Tanaka scheme for two-phase composite materials presented in Mercier et al. (2019).

For a given family of slip systems (a single family is considered for FCC metals), the evolution of the critical resolved shear stress $\tau_c^{r,g}$ is governed by the following hardening law:

$$\tau_{\mathrm{c}}^{r,g} = \tau_{\mathrm{c}}^0 + h_1 \gamma^g + \left(\tau_{\mathrm{sat}} - \tau_{\mathrm{c}}^0\right)\left(1 - e^{-h_{\mathrm{b}}\gamma^g}\right), \tag{11}$$

where $\gamma^g = \int_0^t \dot{\gamma}^g dt$ (with $\dot{\gamma}^g = \sum_r |\dot{\gamma}^{r,g}|$) is the accumulated shear in the grain. $\tau_{\mathrm{c}}^0, \tau_{\mathrm{sat}}, h_1, h_b$ are material parameters. The law (11), similar to a Voce law, combines an exponential term which saturates at large accumulated shear and a linear contribution, see for instance Zecevic and Lebensohn (2020). The multicomponent Ohno-Wang kinematic hardening law (Ohno and Wang, 1993) is also prescribed, namely:

$$\dot{\chi}^{r,g} = \sum_{i=1}^{M} \dot{\chi}_i^{r,g} \quad \text{with} \quad \dot{\chi}_i^{r,g} = h_{\mathrm{k}i}\dot{\gamma}^{r,g} - h_{\mathrm{kb}i}\,|\dot{\gamma}^{r,g}| \left(\frac{\chi^{r,g} h_{\mathrm{kb}i}}{h_{\mathrm{k}i}}\right)^{h_{\mathrm{m}i}}, \tag{12}$$

where M is the total number of components adopted to model the backstress. Other models for kinematic hardening are available in the literature. Material parameters depend upon the slip system family. For FCC materials, only one family of slip systems is considered here. Therefore, one has to define only three coefficients in Eq. (12)

for each component of the kinematic hardening law. In total, we have to determine $3M$ parameters to define the kinematic hardening law and 4 additional ones for the isotropic hardening law.

The crystal plasticity model used in the present work is standard and well set within the community. A discussion on the model formulations and physical meaning of respective parameters can be found in seminal papers (e.g. Asaro and Needleman (1985), Hennessey et al. (2017)). It should be stressed that the main goal of our paper is not to develop a new constitutive model for single grain. Instead, we are focusing on a new averaging scheme enabling micro-macro transition between the level of the single grain and the macro-level (with the specification of a constitutive behavior for the polycrystal, see next section) and its validation as concerns the prediction of the macroscopic response of ED copper. Note also that a first validation stage is proposed in Appendix C where the benchmark of Lebensohn et al. (2012) is adopted for that purpose.

3.2 Elastic-viscoplastic self-consistent model

The goal of this section is to formulate a new elastic-viscoplastic self-consistent scheme for polycrystalline materials and to adopt it for the predictions of the overall response for electrodeposited copper, see Fig. 9. As discussed in the introduction, several self-consistent schemes for elastic-viscoplastic materials (EVPSC) have been proposed in the literature. One can mention for instance Abdul-Latif et al. (1998), Wang et al. (2010a), Kowalczyk-Gajewska and Petryk (2011) or Mareau and Berbenni (2015) among others.

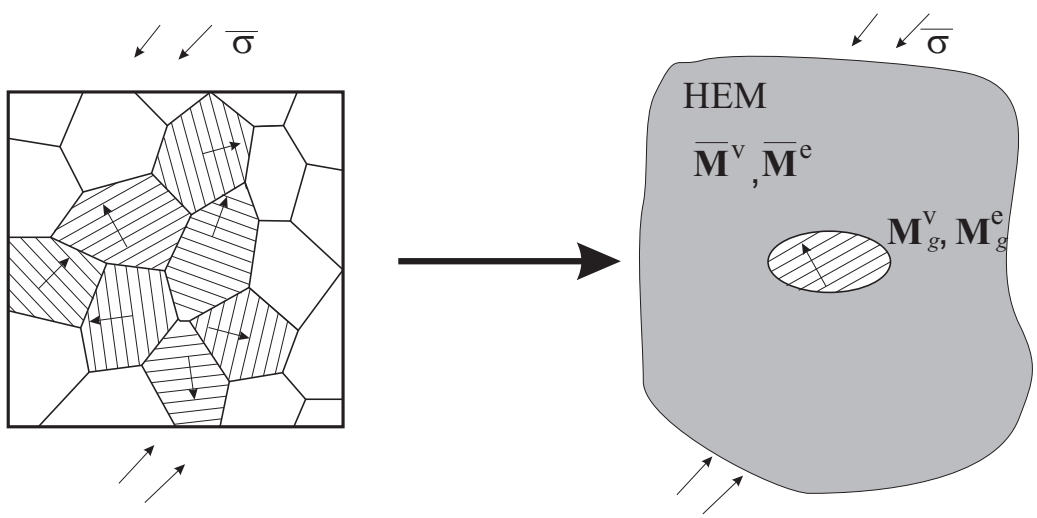

Figure 9: Self-consistent averaging scheme for polycrystal.

The proposed EVPSC scheme relies on the tangent additive interaction law proposed by Molinari et al. (1997) or Molinari (2002):

$$\dot{\boldsymbol{\varepsilon}}_g - \dot{\bar{\boldsymbol{\varepsilon}}} = -\bar{\mathbf{M}}^{\mathrm{e}}_* \cdot (\dot{\boldsymbol{\sigma}}_g - \dot{\bar{\boldsymbol{\sigma}}}) - \bar{\mathbf{M}}^{\mathrm{v}}_* \cdot (\boldsymbol{\sigma}_g - \bar{\boldsymbol{\sigma}}) \,, \tag{13}$$

where $\dot{\bar{\boldsymbol{\varepsilon}}}$ and $\bar{\boldsymbol{\sigma}}$ denote here the overall strain rate and stress, since in the present approach, all inclusions representative of each grain will be considered as spherical. In Eq.(13), $\bar{\mathbf{M}}^{\mathrm{v}}_*$ and $\bar{\mathbf{M}}^{\mathrm{e}}_*$ are fourth order tensors calculated as described in the next paragraphs.

The tensor $\bar{\mathbf{M}}^{\mathrm{v}}_*$ is the fourth order inverse Hill tensor for a purely viscous problem obtained with use of the overall effective viscous stiffness $\bar{\mathbf{A}}^{\mathrm{v}} = (\bar{\mathbf{M}}^{\mathrm{v}})^{-1}$. According to the self-consistent scale transition rule, $\bar{\mathbf{M}}^{\mathrm{v}}$ is

given by the formula (see Hutchinson (1976)):

$$\bar{\mathbf{M}}^{\mathrm{v}} = \langle \mathbf{M}_g^{\mathrm{v}} \circ \mathbf{B}_g^{\mathrm{v}} \rangle \,, \tag{14}$$

where the tangent local viscous compliance $\mathbf{M}_g^{\mathrm{v}}$ provided in Eq. (10), depends on the grain orientation and current values of the mechanical fields in the grain. It must be updated during the calculation process. $\langle \cdot \rangle$ denotes the volume averaging over the representative polycrystalline aggregate and $\circ$ stands for the double contraction of two fourth-order tensors $\mathbf{A}$ and $\mathbf{B}$, which in the index notation gives another fourth-order tensor with components $A_{ijkl}B_{klmn}$. $\mathbf{B}_g^{\mathrm{v}}$ is the respective viscous stress localization tensor calculated as:

$$\mathbf{B}_g^{\mathrm{v}} = (\bar{\mathbf{M}}_*^{\mathrm{v}} + \mathbf{M}_g^{\mathrm{v}})^{-1} \circ (\bar{\mathbf{M}}_*^{\mathrm{v}} + \bar{\mathbf{M}}^{\mathrm{v}}). \tag{15}$$

The fourth-order inverse Hill tensor $\bar{\mathbf{M}}_*^{\mathrm{e}}$ for pure elasticity present in Eq. (13) is defined similarly to the viscoplastic one $\bar{\mathbf{M}}_*^{\mathrm{v}}$. To do so, the overall effective elastic compliance $\bar{\mathbf{M}}^{\mathrm{e}}$ and the elastic stress localization tensor $\mathbf{B}_g^{\mathrm{e}}$ are obtained based on Eqs (14) and (15) in which superscript v is replaced by e (for corresponding elastic quantities). In general, the tensor $\mathbf{M}_g^{\mathrm{e}}$ represents the anisotropic elastic compliance tensor of the grain which depends only on its orientation, when linear elasticity is considered. Since the present formulation is restricted to a small strain approach (without texture evolution), $\mathbf{M}_g^{\mathrm{e}}$, $\mathbf{B}_g^{\mathrm{e}}$ and $\bar{\mathbf{M}}^{\mathrm{e}}$ are invariant throughout the process and need to be evaluated only once.

The elastic-viscoplastic self-consistent model is completed by the standard relations for overall strain rate and stress in the polycrystalline volume:

$$\dot{\bar{\boldsymbol{\varepsilon}}} = \langle \dot{\boldsymbol{\varepsilon}}_g \rangle \,, \quad \dot{\bar{\boldsymbol{\sigma}}} = \langle \dot{\boldsymbol{\sigma}}_g \rangle \,, \quad \bar{\boldsymbol{\sigma}} = \langle \boldsymbol{\sigma}_g \rangle \,. \tag{16}$$

From the interaction law (13), the elastic-viscoplastic behavior of the grains and the closure relationship (16), the macroscopic response is obtained in a concise elegant form as (see Appendix B):

$$\dot{\bar{\boldsymbol{\varepsilon}}} = \bar{\mathbf{M}}^{\mathrm{e}} \cdot \dot{\bar{\boldsymbol{\sigma}}} + \dot{\bar{\boldsymbol{\varepsilon}}}^{\mathrm{v}}, \quad \text{where} \quad \dot{\bar{\boldsymbol{\varepsilon}}}^{\mathrm{v}} = \left\langle (\mathbf{B}_g^{\mathrm{e}})^T \cdot [\dot{\boldsymbol{\varepsilon}}_g^{\mathrm{v}} + \bar{\mathbf{M}}_*^{\mathrm{v}} \cdot (\boldsymbol{\sigma}_g - \bar{\boldsymbol{\sigma}})] \right\rangle \,. \tag{17}$$

This closed form expression for the macroscopic response of the polycrystal is new and has not been presented before. This is one of the main results of the present paper. Indeed, application to polycrystals of the self-consistent scheme based on the tangent additive interaction law with anisotropic tangent viscoplastic stiffness tensor has been proposed in Wang et al. (2010a). Nevertheless, in their work, the authors postulated a macroscopic response for the polycrystal by enforcing the overall behavior to follow a relationship:

$$\dot{\bar{\boldsymbol{\varepsilon}}} = \bar{\mathbf{M}}^{\mathrm{e}} \cdot \dot{\bar{\boldsymbol{\sigma}}} + \bar{\mathbf{M}}^{\mathrm{v}} \cdot \bar{\boldsymbol{\sigma}} + \dot{\bar{\boldsymbol{\varepsilon}}}_o \tag{18}$$

where the latter term $\dot{\bar{\boldsymbol{\varepsilon}}}_o$ is a back-extrapolated term. With some assumptions, they identified $\bar{\mathbf{M}}^{\mathrm{e}}$, $\bar{\mathbf{M}}^{\mathrm{v}}$ and $\dot{\bar{\boldsymbol{\varepsilon}}}_o$. In our present work, as in Mercier and Molinari (2009), the definition of the back-extrapolated strain rate given in Eq. (3.30c) of Wang et al. (2010a) is not needed. In our work, no assumption is made on the mathematical structure of the macroscopic behavior. Indeed, from Wang et al. (2010a), we could extrapolate by mentioning that some parallelism with a thermo-elastic problem is made, as it was proposed for non-linear elastic (or viscous) problem by Zaoui and Masson (2000). From the point of view of the authors, the difference between our proposition and the one of Wang et al. (2010a) is similar to the difference between the work of Molinari et al. (1987) and Zaoui and Masson (2000). The affine method proposed by Zaoui and Masson (2000) was adopting the interaction proposed by Molinari et al. (1987), see Mercier and Molinari (2009) for explanation. The difference in observed results

is originating from the definition of the overall response of the material. In Molinari et al. (1987), the closure relationship $\bar{\boldsymbol{\sigma}} = \langle \boldsymbol{\sigma}_g \rangle$ was assumed while in Zaoui and Masson (2000), a thermo-elastic analogy was made. During the last two decades, a huge literature was proposed to address the difference between the two approaches for viscoplastic polycrystals.

From the point of view of the authors, Eq. (17) represents an important input towards the understanding of the overall response of elastic-viscoplastic polycrystals (or composite materials) in presence of single grains (or phases) having non-linear Maxwell behavior. One clearly observes that even if the local behavior of the grain is of the Maxwell type, the overall response is more complex as can be seen from its expanded form (39) in Appendix B. One can also easily notice a clear difference between the present self-consistent model and classical self-consistent treatment of elastic-viscoplastic heterogeneous materials by the Kröner-Weng scheme (Weng (1982)). The latter approach is recovered when the interactions between the homogenized matrix and the grain are purely elastic, *i.e.* when $\bar{\mathbf{M}}_*^{\mathrm{v}} = \mathbf{0}$.

3.3 EVPSC implementation

The EVPSC scheme has been developed with a structure similar to the VPSC software of Lebensohn and Tomé (1993). An evolutionary algorithm (EA), similar to the one presented in Frydrych (2017); Frydrych et al. (2020), has been applied for the calibration and optimization of the model parameters. The parameters of the evolutionary algorithm are: number of individuals $N_{\mathrm{ind}} = 100$, number of highest ranked individuals (HRI) in each generation $N_{\mathrm{hri}} = 20$, maximal number of generations $N_{\mathrm{gen}} = 200$ and probability of mutation $P_{\mathrm{mut}} = 0.1$. In addition the algorithm stops if the minimum mean standard deviation among fitness values of the HRIs is lower than 0.001. In order to perform the EA optimization with a reasonable computational cost, the measured texture of Fig. 5 has been discretized into 100 orientations using the ATEX software, Beausir and Fundenberger (2017). Next in the paper, when the parameters are identified, predictions of the behavior are obtained for 1000 grain orientations. It has been checked that for the overall behavior, no significant difference was observed when adopting 100 or 1000 orientations.

The proposed EVPSC model and its implementation have been first tested by adopting the benchmark proposed by Lebensohn et al. (2012). More details are provided in Appendix C. Secondly, the EVPSC is adopted to reproduce experimental results on ED copper. This is the goal of Section 4.

4 Results

The macroscopic elastic coefficients of polycrystalline copper are determined in Section 2 leading to $E_{ED} = 80\mathrm{GPa}$ and $\nu_{ED} = 0.33$. The obtained value of the Young's modulus is significantly smaller as compared to the one obtained using the literature data for copper single crystal and the measured texture. Indeed, based on Lebensohn et al. (2012), the three independent components of the stiffness tensor of copper single crystal are

$$C_{11}^0 = 170.2 \text{ [GPa]}, \quad C_{12}^0 = 114.9 \text{ [GPa]}, \quad C_{44}^0 = 61.0 \text{ [GPa]}. \tag{19}$$

With such elastic stiffness of single crystal and the measured texture, the calculated overall Young's modulus is ca. 130 [GPa]. Therefore, one cannot model the experimental result using the data for single crystal. Nevertheless, such reduction of elastic stiffness was already observed in other studies of electrodeposited copper. In Read et al. (2004) for instance, similar small value of Young's modulus (i.e. ca. 80 GPa) was measured. In order to reproduce

the measured Young's modulus, we decided to apply in the simulations the reduced stiffness tensor, namely

$$\mathbf{A}_g^{\mathrm{e}} = \mu \mathbf{A}_g^{\mathrm{e0}} \tag{20}$$

where $\mathbf{A}_g^{\mathrm{e0}}$ is the tensor of cubic symmetry specified with use of literature data (19), while μ is a reduction parameter accounting for the effect of grain boundaries. In order to obtain the predictions consistent with experiments, $\mu = 0.615$ has been assumed. Note that the elastic anisotropy factor of $\mathbf{A}_g^{\mathrm{e}}$ and $\mathbf{A}_g^{\mathrm{e0}}$ is the same. The motivation behind the relation (20) is to keep the formulation as simple as possible and in the same time consistent with experimental measurements. Another possibility which was also tested, was to assume isotropic elastic stiffness of single crystal based on the measured values of the Young's modulus and Poisson's ratio. It has been observed that for both cases the macroscopic predictions were similar, at least under the assumed parameters. However, due to the substantial difference in elastic compliance between orientations, the activity of local slip systems and the resulting shear accumulated in the grains were affected.

As copper is a face centered cubic (FCC) material, 12 slip systems belonging to a single family are considered. The Ohno-Wang kinematic hardening law given by Eq. (12) with only one component ($M = 1$) is adopted with the same material parameters for all slip systems. Finally, only 7 parameters (namely $\tau_{\mathrm{c}}^0, \tau_{\mathrm{sat}}, h_1, h_{\mathrm{b}}, h_{\mathrm{k1}}, h_{\mathrm{kb1}}, h_{\mathrm{m1}}$) have to be identified.

The evolutionary algorithm described in Section 3.3 is applied to optimize the material parameters of the model described in Section 3.1 for the electrodeposited copper ED. The experimental data adopted for parameter determination are 50 tension-compression cycles with amplitude Ampl. 1. From Section 2, the stress components σ_{11}^{c} and σ_{22}^{c} and the strain components $\varepsilon_{11}^{\mathrm{c}}$ and $\varepsilon_{22}^{\mathrm{c}}$ (equal to the overall strain as mentioned in Eq. (28)) are available at any stage of the deformation process for the copper material. Indeed, $\varepsilon_{11} = \varepsilon_{11}^{\mathrm{c}}$ and $\varepsilon_{22} = \varepsilon_{22}^{\mathrm{c}}$ are measured by digital image correlation (DIC). σ_{11}^{c} is obtained from Eq. (30) and the force measurement. σ_{22}^{c} is estimated from the condition (31). Next, the superscript c designating the stress and strain components in copper is omitted for the sake of brevity.

To determine the parameters of the model, strain components ε_{11} and ε_{22} are imposed and the respective stress components predicted by the self-consistent model are compared to experimental values. Note that ε_{12} component is also measured by DIC technique. However, since it is found as negligibly small as compared to ε_{11} and ε_{22}, in simulations $\varepsilon_{12} = 0$ is prescribed together with $\sigma_{33} = \sigma_{13} = \sigma_{23} = 0$. Moreover, it has been shown in Fig. 4 that the magnitude of σ_{22} is limited when compared to σ_{11}. Therefore, the fitness function is evaluated by comparing only the values of σ_{11} at points where the loading direction changes. Despite σ_{22} is not taken into account in the fitness function, the simulation is driven by specifying both strain components. The established set of parameters of the EVPSC model is shown in Tab. 3. The inverse rate sensitivity parameter is set to $n = 8$ and the reference strain rate $\dot{\gamma}_0 = 10^{-4}\mathrm{s}^{-1}$. It has been checked that adopting $n = 10$ as it is proposed in part of the literature for self-consistent scheme (*i.e.* Segurado et al. (2012) or Zecevic and Lebensohn (2020) for copper also), leads to similar results. In addition, the developed EVPSC software is able to provide results also for larger values of n. For example, predictions conducted with reference parameters provided in Table 3 and $n = 2 \times 8 = 16$ were obtained without numerical difficulties for amplitude Ampl. 1. On overall, the numerical efficiency of the code is comparable in this respect with the classical VPSC code, since as concerns the non-linear viscoplastic part of the response and the update of the local crystal plasticity variables similar procedures are used.

Fig. 10a shows the resulting longitudinal stress-strain curves for the first and 50th cycles. A comparison against the experimental data of Fig. 4 is also demonstrated. As parameters are fitted on this experimental data set, of course, a good agreement is observed. Fig. 10b shows the predicted results for the amplitude Ampl. 2.

The same set of parameters is applied. The predictions are compared to the respective cyclic experimental stress-strain response of Fig. 4. A satisfactory agreement with experimental results is still observed. It is found in Fig. 10b that the model underestimates the stress level during the first loading stage. This is the result of the larger stress identified in experiment for Ampl. 2 as seen in Fig. 4 and related to the scatter of ED copper properties between samples resulting from the process of electrodeposition. As the strain amplitude Ampl. 2 is limited, the stabilized cycle is also not as clearly defined as for the largest amplitude. Therefore, the predictions cannot be as perfect as for cycle Ampl. 1. It is also important to mention that predicting the elastic-viscoplastic response of an aggregate for limited strain amplitude is also more challenging when a mean-field approach is used. This was also observed in the work of Czarnota et al. (2015) where results of FE calculations on RVE of composite materials (matrix+inclusions) were compared with the predictions of the additive tangent Mori-Tanaka approach.

For both amplitudes 1 and 2, it is observed that the shape of the cycle evolves slightly after few cycles. Table 4 presents the stress and strain amplitudes for the 10th, 20th up to 50th cycles and Ampl. 1 loading. The stress (respectively strain) amplitude is defined as $|\sigma_{11}^{max} - \sigma_{11}^{min}|$ (respectively $|\varepsilon_{11}^{max} - \varepsilon_{11}^{min}|$) for a given cycle. We clearly observe that amplitudes in stress and strain are stabilized early in the cyclic process. Owing to the value of parameter $h_{\mathrm{b}} = 58.1$, the exponential term in the isotropic hardening law given by Eq. (11) is saturating for low accumulated plastic shear strain. Only the linear contribution pertains. But with such a small value for $h_1 = 2.5$ MPa, this linear isotropic hardening contribution has almost no effect for the present loading conditions. Therefore, for the analyzed ED copper, the kinematic hardening contribution is by far the most important one, the isotropic part of hardening being almost negligible after few cycles.

τ_{c}^0 [MPa]	τ_{sat} [MPa]	h_1 [MPa]	h_{b} [-]	h_{k1} [MPa]	h_{kb1} [MPa]	h_{km1} [-]
38.4	41.0	2.5	58.1	26537	579	3.2

Table 3: Parameters of the EVPSC model established using evolutionary algorithm for electrodeposited ED copper.

Cycle number	Strain amplitude (exp) $[10^{-3}]$	Stress amplitude (exp) [MPa]	Stress amplitude (model) [MPa]
10	4.55	304	304
20	4.57	303	307
30	4.57	305	305
40	4.56	306	304
50	4.54	304	306

Table 4: Evolution of the stress and strain amplitudes for different cycles. Data are reported only every ten cycles. Ampl. 1 loading is considered.

With the EVPSC scheme, one can predict the overall stress-strain response. This could also have been carried out via for instance a phenomenological approach based on the work of Chaboche (1991), see also Ohno and Wang (1993). However, with a mean field approach, one can also obtain information at the level of the grain (restricted to the average quantities). Fig. 11a presents the probability density function of normalized plastic shear strain Γ^g accumulated in a given grain g throughout the whole process. It is defined as the ratio $\gamma^g/\langle\gamma^g\rangle$, where γ^g is the shear strain accumulated in a particular grain g ($\gamma^g = \int_0^T \dot{\gamma}^g dt$, where T is the duration of the whole simulation) and $\langle\gamma^g\rangle$ is the mean value over all grains. For amplitude Ampl. 1 (resp. Ampl. 2), the mean value is $\langle\gamma^g\rangle = 0.29$

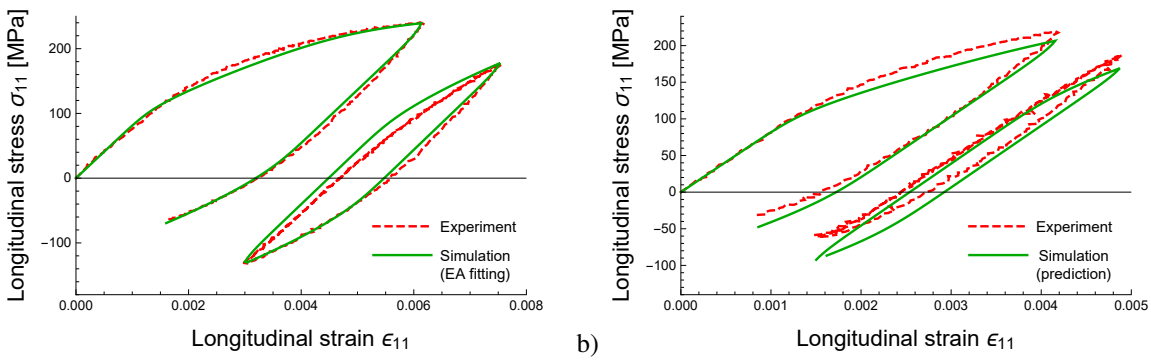

Figure 10: Results of the EVPSC model with the parameters optimized based on experiments: 1st and 50th cycles with amplitude (a) Ampl. 1, (b) Ampl. 2.

(resp. $\langle\gamma^g\rangle = 0.11$). It is seen that for Ampl. 2 condition the scatter in Γ^g is larger. Some grains accumulate only half of the mean value while some grains will accumulate almost 1.5 of the mean value $\langle\gamma^g\rangle$. When considering Ampl. 1 loading (induced by an overall larger stress), it is seen that the distribution is narrower. No grain will remain elastic and the normalized plastic shear strain Γ^g over the whole process is in the range $[0.8 - 1.3]$. This observation was already mentioned elsewhere in the literature, for instance in Sauzay et al. (2010) for polycrystals and in Czarnota et al. (2015) in the context of cyclic behavior of two-phase composite having elastic-viscoplastic behavior.

Fig. 11b depicts the cumulative probability as a function of the normalized accumulated plastic shear strain Γ^g. As observed in Fig. 11a for the largest amplitude Ampl. 1, almost no grain has a normalized plastic shear strain below 0.8, whereas for the smallest amplitude Ampl. 2, more than twenty percent of the grains have such a normalized plastic shear strain or a smaller one. In Fig. 11, five particular grain orientations are selected (greek letters). The orientations are chosen based on their Γ^g value. The orientation α (respectively ω) is representative of the grain having the smallest (respectively largest) plastic activity accumulated over the entire deformation with amplitude Ampl. 1. The third one (δ) corresponds to the mean. Orientation β (respectively η) is located between α and δ (respectively δ and ω) and has the accumulated plastic shear almost equal to $(\Gamma^\alpha+\Gamma^\delta)/2$ (resp. $(\Gamma^\delta+\Gamma^\omega)/2$). It can be also seen in Fig. 11 that for amplitude Ampl. 2, the difference or scatter in plastic activities of these five grains is quite different to the situation observed for Ampl. 1. With larger strain amplitude, the number of slip systems activated during the cyclic loading is larger, and the intensity is also increased.

or.	ϕ_1	Φ	ϕ_2	$\dot{\gamma}^{max,g}$ [1/s]
α	217.29°	75.29°	17.63°	$1.24 \cdot 10^{-4}$
β	19.91°	49.05°	38.73°	$1.18 \cdot 10^{-4}$
δ	349.28°	57.13°	29.87°	$1.62 \cdot 10^{-4}$
η	332.7°	74.22°	47.79°	$1.35 \cdot 10^{-4}$
ω	174.79°	84.13°	45.07°	$0.95 \cdot 10^{-4}$

Table 5: Euler angles of the orientations selected so as their value of Γ^g in the simulation for amplitude Ampl. 1 is the closest one to Γ^g_{min} (*i.e.* α), Γ^g_{max} (*i.e.* ω), Γ^g_{mean} (*i.e.* δ) and is an average of Γ^g_{min} and Γ^g_{mean} *i.e.* (β) or Γ^g_{max} and Γ^g_{mean} (*i.e.*η), see Fig. 11. The corresponding maximum value of the shear rate on slip systems during the last cycle $\dot{\gamma}^{max,g}$ is also reported.

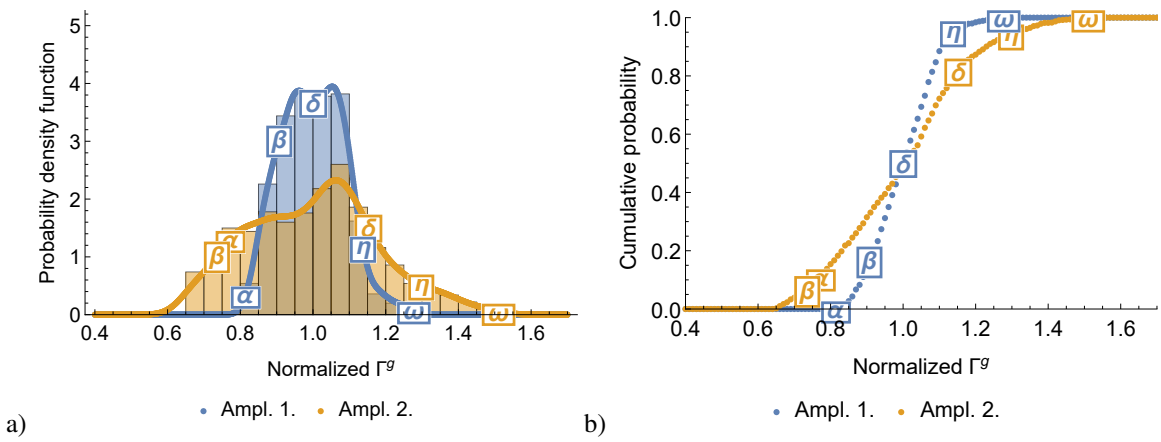

Figure 11: a) Probability density function for the normalized plastic shear strain Γ^g accumulated during the whole deformation. b) Cumulative probability of normalized Γ^g for the two loading conditions. ED copper is considered here. EVPSC predictions are performed with 1000 grains. Material parameters are listed in Table 3.

Fig. 12 presents the intensity of the shear strain γ^g accumulated over the whole deformation for Ampl. 1 as a function of the grain orientation. The position of a respective point in this inverse pole figure provides the orientation of the tensile axis (*i.e.* x axis) with respect to the local crystal axes of the grain g. The positions of the five particular orientations selected in Fig. 11 (see Tab. 5) are also added. The maximum plastic activity is encountered precisely for the grain labelled ω.

It is observed that on average, grains with (100) orientation parallel to x-axis are accumulating more plasticity, while grains with (111) orientation are less active in this respect. These trends are classicaly expected, since (100) and (111) orientations are those of high and low Schmid factor respectively, Kocks et al. (2000). However, the intensity of this trend, and so the variation of the shear strain is strongly affected by the elastic anisotropy parameter $A = \frac{2C_{44}}{C_{11}-C_{12}}$. It has been checked that for grains with (100) orientation parallel to x-axis, the maximum shear strain is almost twice the value when $A = 0.5$ (for respective set of elastic constants see Appendix C) when compared to $A = 2.2$ for the reference set (19). Elastic isotropy produces intermediate results in this respect. There is no decisive trend for grains with (110) orientation parallel to x-axis. Indeed grain ω which presents the maximum γ^g, is located in this orientation area while some other grains with close orientations have small plastic activities (blue color).

The accumulated shear strain during the whole process is the result of the plastic activity on 12 slip systems. Next, the time evolution of the plastic activity on each slip system for five selected orientations is analyzed. It has been checked that the scatter in plastic strain accumulated during the whole process for five selected grains is similar to the situation existing during the last cycle. Indeed, an almost stabilized cycle is observed after few cycles. Fig. 13a presents the normalized shear strain rate $\dot{\gamma}^{r,g}/\dot{\gamma}^{max,g}$ as a function of time for orientation α (the one having the lowest Γ^g as shown in Fig. 11). Results are presented during $45s$, duration of the last cycle. The shear rate $\dot{\gamma}^{r,g}$ in grain g for the slip system r is defined by Eq. (8) and $\dot{\gamma}^{max,g}$ represents the maximum shear rate over all slip systems in grain g obtained during the last cycle. Table 5 provides the corresponding values of $\dot{\gamma}^{max,g}$ for the five selected grains. For grain α, $\dot{\gamma}^{max,\alpha} = 1.24\ 10^{-4}$ [1/s] for system $(111)\,[\bar{1}01]$. Plasticity is mostly developed on two slip systems: $(111)\,[\bar{1}01]$ and $(111)\,[0\bar{1}1]$. For these two systems, the duration of significant activities is around $30s$. One can also observe that secondary slip systems are activated with a reduced intensity

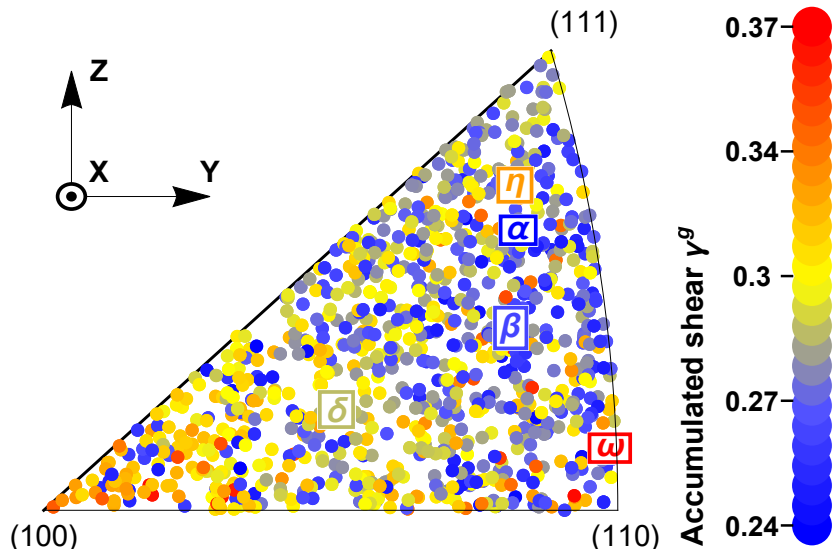

Figure 12: Accumulated plastic shear γ^g for the 1000 grains for ED copper, accumulated during the whole deformation process with Ampl. 1. The position of a respective point in this inverse pole figure provides the orientation of the tensile axis (*i.e.* x axis) with respect to the local crystal axes of grain g. The grain ω is labelled in red, meaning that the accumulated plastic shear is maximum for this orientation.

of around 40% when compared to the two previous ones. Fig.13a) shows also the associated backstress defined in Eq. (12). The most active slip system presents also the largest variation of the backstress $\chi^{r,g}$ during the cycle, from 10 MPa to -25 MPa. For a slip system without any plastic activity during the last cycle, the backstress is unchanged during the cycle, as a consequence of Eq. (12). On the contrary, non-zero value of the backstress is observed for some slip systems, which are inactive during the last cycle. Therefore, they were active in previous cycles.

Fig. 13b presents similarly the situation in terms of normalized shear rate for the grain β. It was shown in Fig. 11 that this grain was accumulating more plasticity during the entire deformation than grain α. The maximum shear rate during the $50th$ cycle is $\dot{\gamma}^{max,\beta} = 1.18\ 10^{-4}$ [1/s] and is smaller than for grain α. For this grain 6 systems are active including one slip system of the highest activity during more than $25s$ and five others with smaller activities. 6 slip systems can be considered as inactive.

For grain δ (see Fig. 13c), the plastic shear strain accumulated during cycles is enlarged (when compared to grains α and β, see Fig. 11 a). The maximum accumulated shear strain rate in the most active slip system is the largest among all five considered orientations: $\dot{\gamma}^{max,\delta} = 1.62\ 10^{-4}$ [1/s]. To accommodate large accumulated plasticity, only four slip systems are activated with one system of predominant activity. For grain η (see Fig. 13d), to further accommodate larger plastic strain, also 4 slip systems operate in the grain but the maximum shear strain rate is reduced: $\dot{\gamma}^{max,\eta} = 1.35\ 10^{-4}$ [1/s] because smaller difference in activity of those four systems is observed. For grain ω (see Fig. 13e), the plasticity is again distributed over 4 slip systems. However, the maximum shear strain rate is further reduced with $\dot{\gamma}^{max,\omega} = 0.95\ 10^{-4}$ [1/s] because those four systems are active with the same duration and intensity. Moreover, for the most active slip systems of grains β, δ, η and ω, it has been observed (results not presented) that the corresponding backstress is varying during the cycle from positive to negative value and vice versa. The plateau regime for the backstress corresponds to an elastic response at the level of the slip system.

It has been checked (results not presented here) that by adopting $n = 10$ for the inverse strain rate sensitivity, the situation depicted in Fig. 13 was slightly modified. Little changes in the maximum shear rate are found. For instance, for $n = 10$, the following values are: $\dot{\gamma}^{max,\alpha} = 1.26\ 10^{-4}$ [1/s], $\dot{\gamma}^{max,\beta} = 1.23\ 10^{-4}$ [1/s], $\dot{\gamma}^{max,\delta} = 1.67\ 10^{-4}$ [1/s], $\dot{\gamma}^{max,\eta} = 1.43\ 10^{-4}$ [1/s] and $\dot{\gamma}^{max,\omega} = 0.97\ 10^{-4}$ [1/s]. A six percent maximum difference is seen for orientation η.

It has been checked (results not presented here) that for the strain amplitude Ampl. 2, the activity on slip systems is quite identical for grains α and β. As for Ampl. 1, one slip system is really active, with a larger intensity for grain α. But secondary slip systems are developing plasticity only slightly. As a consequence, the accumulated plastic shear strain Γ^{α} becomes larger than Γ^{β} for Ampl. 2 during the last cycle and also during the whole deformation process. This explains the change of position of these two grains in Fig. 11 displaying the density function of normalized shear strain.

To summarize the observation displayed in Fig. 13, for a given loading condition, a strong intergranular heterogeneity in plastic shear strain is developed. Depending on the orientation, from one to six slip systems are significantly activated.

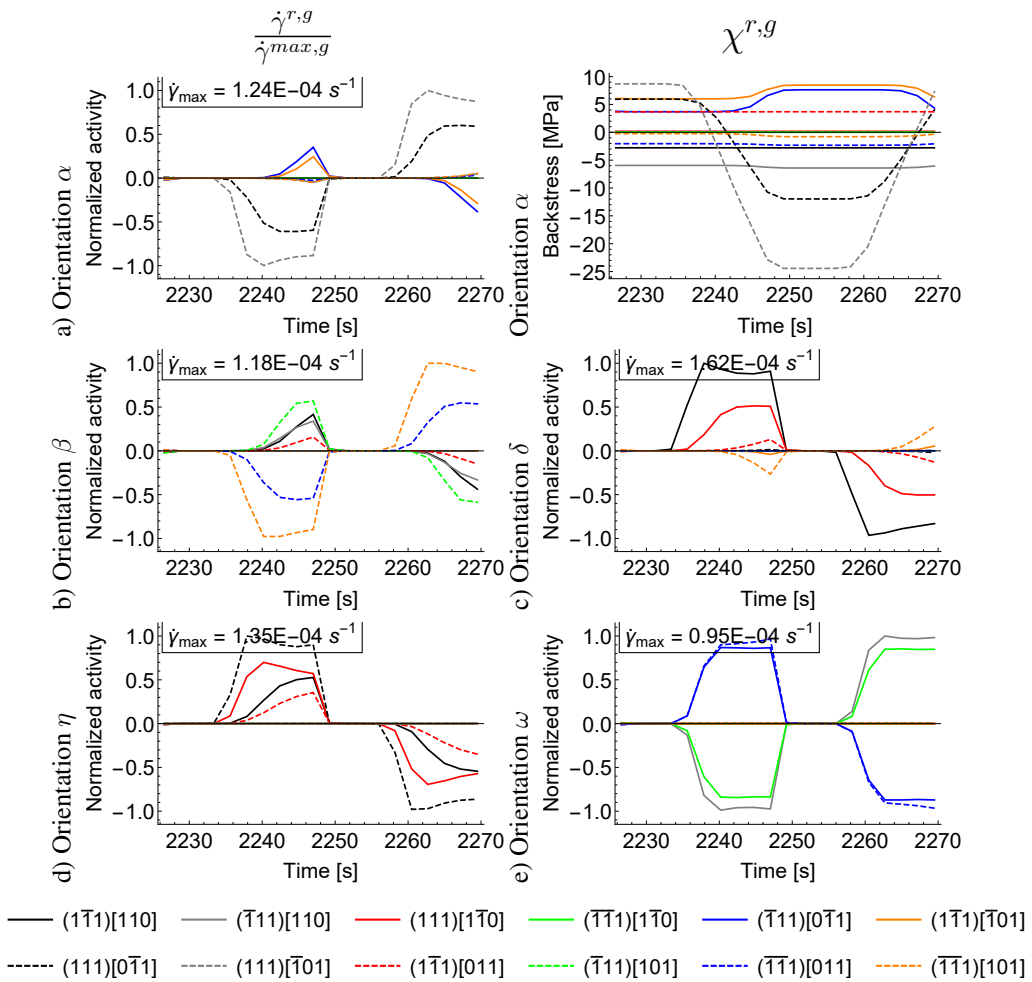

Figure 13: Time evolution during the last cycle of normalized shear strain rate $\dot{\gamma}^{r,g}/\dot{\gamma}^{max,g}$. Results are presented for orientations defined in Tab. 5 a) α, b) β, c) δ, d) η and e) ω. For orientation α, the backstress $\chi^{r,g}$ evolution is also shown. Amplitude Ampl. 1 is considered here. Material parameters are listed in Table 3.

5 Discussion on grain size effect

As discussed in Section 2 the mean grain size of electrodeposited copper is relatively small, while some scatter in grain sizes is also seen. Therefore one can expect a Hall-Petch-type strengthening between the grains. In order to assess this effect on the local response of electrodeposited copper, the critical shear stress for the single grain is modified as follows

$$\tau_{\mathrm{c}}^{r,g} = \tau_{\mathrm{c}}^{0} + \frac{\Pi}{\sqrt{d^g}} + h_1\gamma^g + \left(\tau_{\mathrm{sat}} - \tau_{\mathrm{c}}^{0}\right)\left(1 - e^{-h_{\mathrm{b}}\gamma^g}\right), \tag{21}$$

where d^g is the grain diameter and $\Pi = 8.13\ \mathrm{MPa}\sqrt{\mu\mathrm{m}}$ is taken from Abdul-Latif et al. (2018).

In order to compare the results with the original model without grain size effect, the values of τ_{c}^{0} and τ_{sat} have been recalculated as follows:

$$\tau_{\mathrm{c}}^{0(\mathrm{new})} + \frac{\Pi}{\sqrt{D_A}} = \tau_{\mathrm{c}}^{0} \quad \text{and} \quad {\tau_{\mathrm{sat}}}^{(\mathrm{new})} + \frac{\Pi}{\sqrt{\mathrm{D_A}}} = \tau_{\mathrm{sat}}, \tag{22}$$

where D_A is the area-weighted mean grain size, while other material parameters are still given in Table 3. A second possibility could have been considered by selecting D_N instead of D_A for the scaling of new parameters by Eq. (22). It has been verified that the difference in the predicted overall response shown in Fig. 10 is barely discernible (results not shown here). For a fair comparison, the microstructure data based on the EBSD measurements containing the grain orientation and the corresponding grain size, have been used here (note that results in the previous section were obtained using XRD data for texture). From the grain size in the EBSD map, the volume fraction of a given orientation in the considered aggregate has been calculated.

In Fig. 14 results related to the local response are compared for the model without and with grain size effect. It is seen that with a new set of texture data, based on EBSD measurements, results for the model without grain size are similar to those presented in the previous section based on the XRD texture data. Adding the size effect introduces a larger scatter in normalized accumulated plastic shear Γ^g among the grains and diminishes the correlation between the orientation and Γ^g. Note that when we add the size effect, contrary to the original model, some grains may remain elastic during the process as Γ^g is varying in the range $[0, 2]$ for Ampl. 1 and $[0, 2.5]$ for Ampl. 2. To validate the presence (or not) of the Hall-Petch term in the modeling, further investigations on the slip system activities at the level of the grains would be necessary and be carried out in a future work.

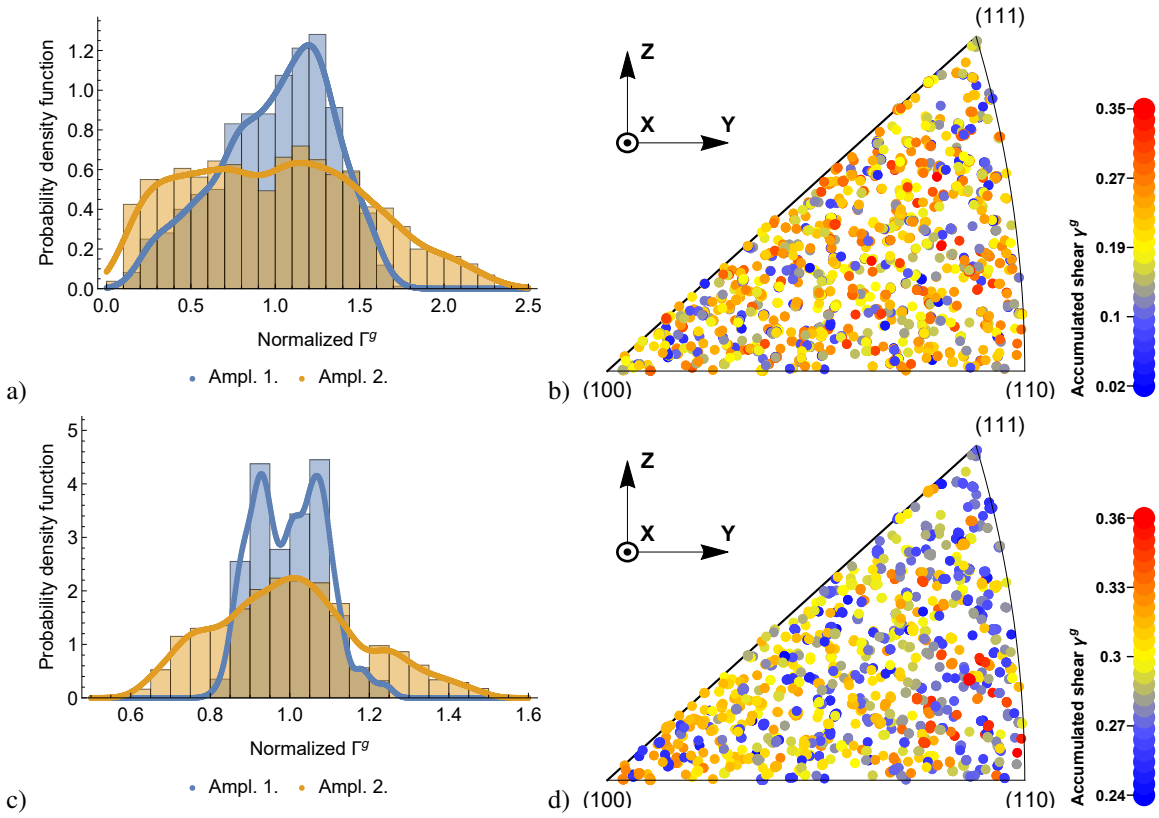

Figure 14: Left column: Probability density function for the normalized plastic shear strain Γ^g accumulated during the whole deformation (a) $D = D_A$ (c) $D = \infty$ (without Hall Petch effect). Right column: Accumulated plastic shear γ^g for 1626 grains for ED copper, during the whole deformation process with Ampl. 1 (b) $D = D_A$ (d) $D = \infty$ (without Hall Petch effect). The position of a respective point in this inverse pole figure provides the orientation of the tensile axis (*i.e.* x axis) with respect to the local crystal axes of grain g. Note that, the texture data are now taken from EBSD measurements, while in Fig. 12, the texture was obtained from XRD measurements.

6 Summary and conclusions

The goal of the present work is to propose a new multi-scale approach for elastic-viscoplastic polycrystalline materials. The model is applied to electrodeposited copper whose macroscopic cyclic behavior has been accurately captured by the experimental procedure of the present work. For that purpose, a specific specimen is adopted where a compliant core is supporting copper films. In the course of tensile loadings-unloadings on test specimens, copper films experience tension compression cycles. As the number of cycles increases, a combined isotropic kinematic hardening is developing.

As expected for electrodeposited copper, the texture is rather weak. From EBSD map, the distribution of grain size is identified. No correlation between grain orientations and grain sizes has been observed. From the EBSD image analysis, it is found that the number of grains in the thickness is significant for the film thickness considered in the present paper ($45\mu m$) what justifies the use of the representative volume element and application of the mean-field approach.

The new elastic-viscoplastic self-consistent scheme (EVPSC) is based on the tangent additive interaction law of Molinari (2002). A small strain formalism is adopted. One of the main outcomes of the present paper is the definition of the overall response of the aggregate in a simple and meaningful expression. Even though the local behavior of the phases is of the Maxwell type, the overall response is more complex. This new macroscopic constitutive behavior is different from other models of the literature, even for those who adopted the same interaction law, see for instance Wang et al. (2010a). From the implementation point of view an access to the overall stress-strain relation enables straightforward application of mixed boundary conditions to the RVE, as required in the present study.

The behavior of each grain is consistent with the rate-dependent crystal plasticity formulation. Kinematic hardening is accounted for at the level of the slip system and transferred to the macroscopic scale by the interaction law and volume averaging. The model parameters are identified via an evolutionary algorithm by comparing the predictions to the identified stress-strain cycles. Owing to the applied identification procedure, the overall response is well captured by the present EVPSC scheme. Natural outcomes of the present approach are the slip system activities. The number of active slip systems is shown to be grain orientation-dependent during stabilized cycles. More interestingly, owing to the dispersion in grain size and the presence of small grains, it is concluded that the shear accumulated in each grain is clearly modified when the Hall-Petch contribution is introduced in the model. Further microstructural investigation would be necessary to validate this finding. It should be stressed that the knowledge of the local heterogeneity of stress and strain is important for a more accurate assessment of PCB reliability.

The present elastic-viscoplastic self-consistent scheme has been adopted for the prediction of the cyclic response of copper but could be also adopted for other polycrystalline materials and any loading conditions.

7 Acknowledgments

The authors thank for the support of Agence Nationale de Recherche through the program Labcom ANR-14-LAB7-0003-01 for the creation of the labcom LEMCI and Région Grand Est with the grant " soutien aux jeunes chercheurs" for Gautier Girard. The financial support of Metz Métropole, of Département de la Moselle, of CIMULEC, SYSTRONIC and CSI SUD OUEST through the NIT foundation is also acknowledged. The support of J. Guyon, O. Perroud, J. Slowensky of LEM3 for texture and EBSD measurements and for helpful discussions

on microstructures are gratefully acknowledged.

A Experimental determination of the copper mechanical response

The considered substrate has an orthotropic elastic behavior. The copper film is considered isotropic (at least in the plane) and perfectly bonded to the substrate. During loading and unloading of the considered specimen along direction 1, both materials (copper and substrate) are in a biaxial stress state, at least because of difference in their Poisson's ratio. It is assumed that plane stress prevails and shear contribution is disregarded. The stress tensor in each material is of the form:

$$\boldsymbol{\sigma} = \begin{bmatrix} \sigma_{11} & 0 & 0 \\ 0 & \sigma_{22} & 0 \\ 0 & 0 & 0 \end{bmatrix}. \tag{23}$$

Note that the overall stress tensor $\boldsymbol{\Sigma}$ is representative of uniaxial tension, so $\Sigma_{11} \neq 0$ and $\Sigma_{22} = 0$.

The substrate has an orthotropic elastic behavior leading to the following link between stress and strain components:

$$\varepsilon_{11}^s = \frac{\sigma_{11}^s - \nu_{12}^s \sigma_{22}^s}{E_1^s}, \tag{24}$$

$$\varepsilon_{22}^s = \frac{\sigma_{22}^s}{E_2^s} - \frac{\nu_{12}^s \sigma_{11}^s}{E_1^s}. \tag{25}$$

Assuming that stress and strain fields are uniform in each phase, the macrostress tensor is linked to the stress in each phase by volume averaging:

$$\Sigma_{11} = \frac{h^c \sigma_{11}^c + h^s \sigma_{11}^s}{h^c + h^s}, \tag{26}$$

$$\Sigma_{22} = \frac{h^c \sigma_{22}^c + h^s \sigma_{22}^s}{h^c + h^s} = 0, \tag{27}$$

where superscripts s and c designate substrate and copper materials, respectively. Remember that h^s represents the thickness of the substrate and h^c the thickness of the two copper layers, see Fig. 1c. Owing to small deformations, it is assumed that h^s and h^c are fixed during loading. Their values are given in Table 1.

The two materials (copper and substrate) are considered perfectly bonded, so that the following relationships between strains hold:

$$\varepsilon_{11}^s = \varepsilon_{11}^c = \varepsilon_{11} \quad \varepsilon_{22}^s = \varepsilon_{22}^c = \varepsilon_{22}, \tag{28}$$

where ε_{11} and ε_{22} are the macroscopic strains in the plane, measured by digital image correlation. During uniaxial loading/unloading described in section 2.1, Σ_{11} is directly related to the measured force F_1:

$$\Sigma_{11} = \frac{F_1}{w(h^c + h^s)}, \tag{29}$$

where w is the width of the gauge section: $w = 15\text{mm}$, as seen in Figure 1. The four unknowns σ_{11}^s, σ_{22}^s, σ_{11}^c and σ_{22}^c are identified by solving the linear system formed by equations (24) to (27). The explicit relations for the stress components in the substrate σ_{11}^s and σ_{22}^s are obtained in a straightforward manner from equations (24) and (25). The stress components in copper are derived by using subsequently Eqs (26) and (27):

$$\sigma_{11}^c = \frac{\Sigma_{11}(h^s + h^c)}{h^c} - \frac{h^s}{h^c}\left(\frac{\varepsilon_{11}(E_1^s)^2 + \varepsilon_{22} E_1^s E_2^s \nu_{12}^s}{E_1^s - E_2^s(\nu_{12}^s)^2}\right), \tag{30}$$

$$\sigma_{22}^c = -\frac{h^s}{h^c}\left(\frac{E_1^s E_2^s(\varepsilon_{22} + \varepsilon_{11}\nu_{12}^s)}{E_1^s - E_2^s(\nu_{12}^s)^2}\right). \tag{31}$$

B Derivation of the overall constitutive relation for the polycrystal

From Eqs (13) and (4), the additive interaction law is written as follows:

$$\dot{\boldsymbol{\varepsilon}}_g^{\mathrm{e}} + \dot{\boldsymbol{\varepsilon}}_g^{\mathrm{v}} - \dot{\bar{\boldsymbol{\varepsilon}}} = -\bar{\mathbf{M}}_*^{\mathrm{e}} \cdot (\dot{\boldsymbol{\sigma}}_g - \dot{\bar{\boldsymbol{\sigma}}}) - \bar{\mathbf{M}}_*^{\mathrm{v}} \cdot (\boldsymbol{\sigma}_g - \bar{\boldsymbol{\sigma}}) \,, \tag{32}$$

From the elastic constitutive law, one gets:

$$(\mathbf{M}_g^{\mathrm{e}} + \bar{\mathbf{M}}_*^{\mathrm{e}}) \cdot \dot{\boldsymbol{\sigma}}_g = (\dot{\bar{\boldsymbol{\varepsilon}}} - \dot{\boldsymbol{\varepsilon}}_g^{\mathrm{v}}) - \bar{\mathbf{M}}_*^{\mathrm{v}} \cdot (\boldsymbol{\sigma}_g - \bar{\boldsymbol{\sigma}}) + \bar{\mathbf{M}}_*^{\mathrm{e}} \cdot \dot{\bar{\boldsymbol{\sigma}}}. \tag{33}$$

The former equation enables to obtain the stress rate in each grain:

$$\dot{\boldsymbol{\sigma}}_g = (\mathbf{M}_g^{\mathrm{e}} + \bar{\mathbf{M}}_*^{\mathrm{e}})^{-1} \circ \bar{\mathbf{M}}_*^{\mathrm{e}} \cdot \dot{\bar{\boldsymbol{\sigma}}} + (\mathbf{M}_g^{\mathrm{e}} + \bar{\mathbf{M}}_*^{\mathrm{e}})^{-1} \cdot [\dot{\bar{\boldsymbol{\varepsilon}}} - \dot{\boldsymbol{\varepsilon}}_g^{\mathrm{v}} - \bar{\mathbf{M}}_*^{\mathrm{v}} \cdot (\boldsymbol{\sigma}_g - \bar{\boldsymbol{\sigma}})]. \tag{34}$$

Owing to Eq. (16) ($\dot{\bar{\boldsymbol{\sigma}}} = \langle \dot{\boldsymbol{\sigma}}_g \rangle$), the overall stress rate is found:

$$\dot{\bar{\boldsymbol{\sigma}}} = \langle (\mathbf{M}_g^{\mathrm{e}} + \bar{\mathbf{M}}_*^{\mathrm{e}})^{-1} \rangle \circ \bar{\mathbf{M}}_*^{\mathrm{e}} \cdot \dot{\bar{\boldsymbol{\sigma}}} + \langle (\mathbf{M}_g^{\mathrm{e}} + \bar{\mathbf{M}}_*^{\mathrm{e}})^{-1} [\dot{\bar{\boldsymbol{\varepsilon}}} - \dot{\boldsymbol{\varepsilon}}_g^{\mathrm{v}} - \bar{\mathbf{M}}_*^{\mathrm{v}} \cdot (\boldsymbol{\sigma}_g - \bar{\boldsymbol{\sigma}})] \rangle. \tag{35}$$

Note that the same inclusion shape for all grains is assumed, so that the Hill tensor is the same for the grains. Therefore, the following relation holds:

$$\left\langle \mathbf{B}_g^{\mathrm{e}} \right\rangle = \left\langle (\mathbf{M}_g^{\mathrm{e}} + \bar{\mathbf{M}}_*^{\mathrm{e}})^{-1} \right\rangle \circ (\bar{\mathbf{M}}^{\mathrm{e}} + \bar{\mathbf{M}}_*^{\mathrm{e}}) = \mathbf{I} \rightarrow \left\langle (\mathbf{M}_g^{\mathrm{e}} + \bar{\mathbf{M}}_*^{\mathrm{e}})^{-1} \right\rangle = (\bar{\mathbf{M}}^{\mathrm{e}} + \bar{\mathbf{M}}_*^{\mathrm{e}})^{-1}. \tag{36}$$

Using Eq. (36), Eq. (35) is re-arranged so that the overall stress rate is now defined as:

$$\dot{\bar{\boldsymbol{\sigma}}} = (\bar{\mathbf{M}}^{\mathrm{e}} + \bar{\mathbf{M}}_*^{\mathrm{e}})^{-1} \circ \bar{\mathbf{M}}_*^{\mathrm{e}} \cdot \dot{\bar{\boldsymbol{\sigma}}} + (\bar{\mathbf{M}}^{\mathrm{e}} + \bar{\mathbf{M}}_*^{\mathrm{e}})^{-1} \cdot \dot{\bar{\boldsymbol{\varepsilon}}} - \langle (\mathbf{M}_g^{\mathrm{e}} + \bar{\mathbf{M}}_*^{\mathrm{e}})^{-1} [\dot{\boldsymbol{\varepsilon}}_g^{\mathrm{v}} + \bar{\mathbf{M}}_*^{\mathrm{v}} \cdot (\boldsymbol{\sigma}_g - \bar{\boldsymbol{\sigma}})] \rangle. \tag{37}$$

By multiplying the left and right-hand sides of Eq. (37) by the tensor $(\bar{\mathbf{M}}^{\mathrm{e}} + \bar{\mathbf{M}}_*^{\mathrm{e}})$ and introducing the definition of $\mathbf{B}_g^{\mathrm{e}}$, one finally gets:

$$\bar{\mathbf{M}}^{\mathrm{e}} \cdot \dot{\bar{\boldsymbol{\sigma}}} = \dot{\bar{\boldsymbol{\varepsilon}}} - \langle (\mathbf{B}_g^{\mathrm{e}})^T \cdot [\dot{\boldsymbol{\varepsilon}}_g^{\mathrm{v}} + \bar{\mathbf{M}}_*^{\mathrm{v}} \cdot (\boldsymbol{\sigma}_g - \bar{\boldsymbol{\sigma}})] \rangle. \tag{38}$$

The above relation coincides with the constitutive equation Eq. (17) of the polycrystal and can be expanded to

$$\dot{\bar{\boldsymbol{\varepsilon}}} = \bar{\mathbf{M}}^{\mathrm{e}} \cdot \dot{\bar{\boldsymbol{\sigma}}} + \left\langle (\mathbf{B}_g^{\mathrm{e}})^T \cdot \dot{\boldsymbol{\varepsilon}}_g^{\mathrm{v}} \right\rangle + \left\langle (\mathbf{B}_g^{\mathrm{e}})^T \circ \bar{\mathbf{M}}_*^{\mathrm{v}} \cdot \boldsymbol{\sigma}_g \right\rangle - \bar{\mathbf{M}}_*^{\mathrm{v}} \cdot \bar{\boldsymbol{\sigma}}. \tag{39}$$

The overall constitutive behavior Eq. (39) can be also deduced, adopting the concept of sequential linearization presented in Kowalczyk-Gajewska and Petryk (2011) when the additional accomodation step is neglected.

C Validation stage through the benchmark of Lebensohn et al. (2012)

Lebensohn et al. (2012) have performed elastic-viscoplastic FFT calculations on polycrystalline copper. The single crystal constitutive relationship is similar to the one considered in Section 3.1 when kinematic hardening is disregarded. Linear hardening is used in Lebensohn et al. (2012) work and can be derived from Eq. (11) by setting $h_b = 0$. The linear hardening coefficient h_1 is ranging from $h_1 = 0$ (perfectly plastic case) to $h_1 = 1000$ MPa. The reference critical resolved shear stress is $\tau_c^0 = 10$ MPa and the inverse of the strain rate sensitivity $n = 10$. The texture is random. The single crystal elastic constants are given in Eq. (19). As FFT calculations are performed up to 0.3% strain, the small strain theory without texture evolution developed in the present work is salient. So the EVPSC scheme is used to reproduce the results of the benchmark proposed in Section 3 of Lebensohn et al.

(2012) with the considered material parameters defined above. In our calculations, the random texture contains 125 orientations.

In the first benchmark, uniaxial tension along x_1 is considered with an applied strain rate $\dot{\varepsilon}_{11} = 1\ \mathrm{s}^{-1}$ and $\sigma_{22} = \sigma_{33} = 0$. No strain hardening is accounted for in this configuration. Fig. 15 a) presents the equivalent stress-strain curve predicted by the EVPSC model and a comparison with the EVP-FFT results of Lebensohn et al. (2012). A fairly good agreement is obtained. Fig. 15 b) displays the evolution of the predicted (instantaneous as denoted by Lebensohn et al. (2012)) transversal to longitudinal strain rate ratio $-\frac{\dot{\varepsilon}_{22}}{\dot{\varepsilon}_{11}}$ and the same (accumulated) ratio for the total strain $-\frac{\varepsilon_{22}}{\varepsilon_{11}}$ during the loading. During elastic deformation, the instantaneous strain rate ratio is close to 0.35 (see bottom dashed line), corresponding to the Poisson's ratio for polycrystalline copper with random texture. This ratio evolves rapidly to reach a plateau value of 0.5 (see top dashed line), as the plastic flow is assumed incompressible. It is interesting to mention that the predicted ratios (instantaneous and accumulated) are in close agreement with the one captured by the reference EVP-FFT calculations.

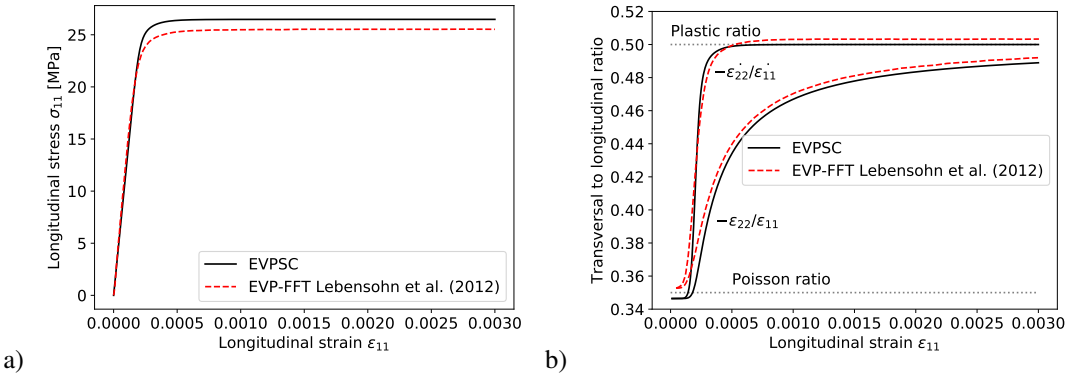

Figure 15: Uniaxial tensile response of polycrystalline copper with random texture. a) Longitudinal stress versus longitudinal strain. b) Evolution of the transversal to longitudinal strain rate $-\frac{\dot{\varepsilon}_{22}}{\dot{\varepsilon}_{11}}$ and strain $-\frac{\varepsilon_{22}}{\varepsilon_{11}}$ ratios. Comparisons are made between predictions of the proposed EVPSC model and reference calculations obtained by EVP-FFT, taken from Lebensohn et al. (2012). The longitudinal strain rate is set to $\dot{\varepsilon}_{11} = 1\ \mathrm{s}^{-1}$. The texture is random.

The second series of tests proposed in Lebensohn et al. (2012) investigates the effects of the applied strain rate and of elastic anisotropy on the overall response. For that purpose, uniaxial tensions are first conducted with longitudinal strain rate varying in the range $[10^{-3}\ \mathrm{s}^{-1},\ 1\ \mathrm{s}^{-1}]$. The hardening coefficient is set to $h_1 = 100$ MPa. It is observed in Fig. 16 a) that the rate effect (with $n = 10$) is well captured by the EVPSC modeling. Lebensohn et al. (2012) investigate also the interplay between elastic and viscoplastic anisotropy. The elastic anisotropy parameter $A = \frac{2C_{44}}{C_{11}-C_{12}}$ is equal to $A = 2.2$ for the reference copper. They define an additional artificial FCC polycrystal having the same initial texture, same viscoplastic response for the single grain (still $h_1 = 100$ MPa) but different single crystal elastic anisotropy. By prescribing $A = 0.5$ and preserving the elastic effective response, the new elastic moduli are: $C_{11} = 233.6$, $C_{12} = 88.2$ and $C_{44} = 33.8$ GPa. Fig. 16 shows that our EVPSC model is also able to capture the overall response given by the EVP-FFT. For instance, a longer elasto-viscoplastic transition with $A = 0.5$ is well predicted. As explained also by Lebensohn et al. (2012), the length of the transient region is a result of the interplay between anisotropy of elastic and viscoplastic properties. In the case of $A = 2.2$ orientations (111), elastically the stiffest, are in the same time those which have the lowest Schmid factor. A reverse situation is found for $A = 0.5$, orientations (111) are in this case the softest elastically. Thus in the second case the time

interval between initiation of yielding for (001) and (111) orientations is longer than in the case of $A = 2.2$. Elastic isotropy produces intermediate results in this respect.

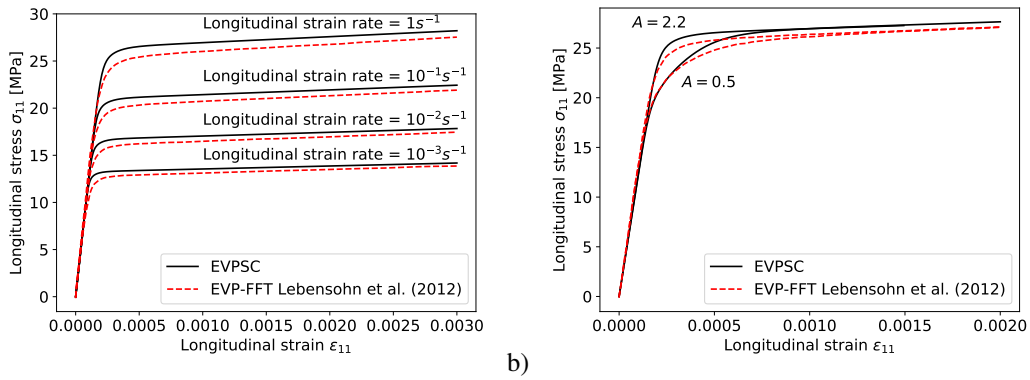

a) b)

Figure 16: Uniaxial stress-strain curves for a) various strain rates in the range $[10^{-3}\ s^{-1},\ 1\ s^{-1}]$ b) two elastic-viscoplastic materials having the same viscoplastic response but different elastic anisotropy: $A = 2.2$ for reference copper and $A = 0.5$ for the articificial FCC poycrystal. The longitudinal strain rate is set to $\dot{\varepsilon}_{11} = 1\ s^{-1}$. Comparisons are made between predictions of the proposed EVPSC model and reference calculations obtained by EVP-FFT, taken from Lebensohn et al. (2012). The hardening coefficient is $h_1 = 100$ MPa. The texture is random.

References

A. Abdul-Latif, J.Ph. Dingli, and K. Saanouni. Modeling of complex cyclic inelasticity in heterogeneous polycrystalline microstructure. *Mechanics of Materials*, 30(4):287 – 305, 1998.

A. Abdul-Latif, A. Kerkour-El Miad, R. Baleh, and H. Garmestani. Modeling the mechanical behavior of heterogeneous ultrafine grained polycrystalline and nanocrystalline fcc metals. *Mechanics of Materials*, 126:1 – 12, 2018.

F. Adzima, T. Balan, P.Y. Manach, N. Bonnet, and L. Tabourot. Crystal plasticity and phenomenological approaches for the simulation of deformation behavior in thin copper alloy sheets. *International Journal of Plasticity*, 94:171 – 191, 2017.

R.J. Asaro and A. Needleman. Overview. texture development and strain-hardening in rate dependent polycrystals. *Acta Met.*, 33:923–953, 1985.

B. Bacroix, S. Queyreau, D. Chaubet, E. Siv, and Th Chauveau. The influence of the cube component on the mechanical behaviour of copper polycrystalline samples in tension. *Acta Materialia*, 160:121–136, 2018.

B. Beausir and J.-J. Fundenberger. Analysis Tools for Electron and X-ray diffraction, ATEX - software, Université de Lorraine, 2017. URL `www.atex-software.eu`.

N. Bozzolo and M. Bernacki. Viewpoint on the formation and evolution of annealing twins during thermomechanical processing of fcc metals and alloys. *Metallurgical and Materials Transactions A*, 51:2665 – 2684, 2020.

T. E. Buchheit, R. J. Bourcier, G. W. Wellman, and M. K. Neilsen. Capturing the influence of surface constraints in small and thin samples using polycrystalline plasticity theory. *Modelling and Simulation in Materials Science and Engineering*, 5(4):421–437, 1997.

J.L. Chaboche. On some modifications of kinematic hardening to improve the description of ratchetting effects. *International Journal of Plasticity*, 7:661–678, 1991.

A. Cruzado, S. Lucarini, J. LLorca, and J. Segurado. Crystal plasticity simulation of the effect of grain size on the fatigue behavior of polycrystalline inconel 718. *International Journal of Fatigue*, 113:236 – 245, 2018.

C. Czarnota, K. Kowalczyk-Gajewska, A. Salahouelhadj, M. Martiny, and S. Mercier. Modeling of the cyclic behavior of elastic–viscoplastic composites by the additive tangent Mori–Tanaka approach and validation by finite element calculations. *International Journal of Solids and Structures*, 56-57:96 – 117, 2015.

H. Farooq, G. Cailletaud, S. Forest, and D. Ryckelynck. Crystal plasticity modeling of the cyclic behavior of polycrystalline aggregates under non-symmetric uniaxial loading: Global and local analyses. *International Journal of Plasticity*, 126:102619, 2020.

K. Fellner, P.F. Fuchs, G. Pinter, T. Antretter, and T. Krivec. Method development for the cyclic characterization of thin copper layers for pcb applications. *Circuit World*, 40(2):53–60, 2014.

K. Fellner, T. Antretter, P.F. Fuchs, and T. Pélisset. Cyclic mechanical behavior of thin layers of copper: A theoretical and numerical study. *The Journal of Strain Analysis for Engineering Design*, 51(2):161–169, 2016.

K. Frydrych. *Modelling of microstructure evolution of high specific strength metals subjected to severe plastic deformation processes.* Ph.D. thesis, Institute of Fundamental Technological Research, Polish Academy of Sciences, Warsaw, Poland, 2017. in Polish.

K. Frydrych, M. Maj, L. Urbański, and K. Kowalczyk-Gajewska. Twinning-induced anisotropy of mechanical response of AZ31B extruded rodes. *Materials Science and Engineering: A*, 771:138610, 2020.

C. Fu, I.C. Ume, and D.L. McDowell. Thermal stress and fatigue analysis of plated-through holes using an internal state variable constitutive model. *Finite Elements in Analysis and Design*, 30:1–17, 1998.

K. Haldrup, R.D. McGinty, and D.L. McDowell. Effects of constraints on lattice re-orientation and strain in polycrystal plasticity simulations. *Computational Materials Science*, 44(4):1198 – 1207, 2009.

Z. Hashin. Viscoelastic fiber reinforced materials. *AIAA Journal*, 4:1411, 1966.

C. Hennessey, G. M. Castelluccio, and D. L. McDowell. Sensitivity of polycrystal plasticity to slip system kinematic hardening laws for al 7075-t6. *Materials Science and Engineering: A*, 687:241 – 248, 2017.

J. W. Hutchinson. Bounds and self-consistent estimates for creep of polycrystalline materials. *Proc. Roy. Soc. Lond. A*, 348:101–127, 1976.

C. Keller and E. Hug. Kocks-Mecking analysis of the size effects on the mechanical behavior of nickel polycrystals. *International Journal of Plasticity*, 98:106 – 122, 2017.

U. F. Kocks, C. N. Tomé, and H.-R. Wenk. *Texture and Anisotropy*. Cambridge University Press, II edition, 2000.

K. Kowalczyk-Gajewska. Micromechanical modelling of metals and alloys of high specific strength. *IFTR Reports 1/2011*, pages 1–299, 2011.

K. Kowalczyk-Gajewska and H. Petryk. Sequential linearization method for viscous/elastic heterogeneous materials. *Eur. J. Mech. Solids/A*, 30:650–664, 2011.

O Kraft, R Schwaiger, and P Wellner. Fatigue in thin films: lifetime and damage formation. *Materials Science and Engineering: A*, 319-321:919 – 923, 2001.

R. A. Lebensohn and C. N. Tomé. A self-consistent anisotropic approach for the simulation of plastic deformation and texture development of polycrystals: Application to zirconium alloys. *Acta Metall. Mater.*, 41:2611–2624, 1993.

R. A. Lebensohn, A. K. Kanjarla, and P. Eisenlohr. An elasto-viscoplastic formulation based on fast fourier transforms for the prediction of micromechanical fields in polycrystalline materials. *International Journal of Plasticity*, 32-33:59 – 69, 2012.

Y Liu, P Gilormini, and P Ponte Castañeda. Variational self-consistent estimates for texture evolution in viscoplastic polycrystals. *Acta Materialia*, 51(18):5425 – 5437, 2003.

F. Macionczyk and W. Brückner. Tensile testing of AlCu thin films on polyimide foils. *Journal of Applied Physics*, 86:4922–4929, 1999.

C. Mareau and S. Berbenni. An affine formulation for the self-consistent modeling of elasto-viscoplastic heterogeneous materials based on the translated field method. *International Journal of Plasticity*, 64:134 – 150, 2015.

R. Masson and A. Zaoui. Self-consistent estimates of the rate-dependent elasto-plastic behaviour of polycrystalline materials. *J. Mech. Phys. Solids*, 47:1543–1568, 1999.

S. Mercier and A. Molinari. Homogenization of elastic-viscoplastic heterogeneous materials: Self-consistent and Mori-Tanaka schemes. *Int. J. Plast.*, 25:1024–1048, 2009.

S. Mercier, N. Jacques, and A. Molinari. Validation of an interaction law for the Eshelby inclusion problem in elasto-viscoplasticity. *Int. J. Solids Structures*, 42:1923–1941, 2005.

S. Mercier, K. Kowalczyk-Gajewska, and C. Czarnota. Effective behavior of composites with combined kinematic and isotropic hardening based on additive tangent Mori–Tanaka scheme. *Composites Part B: Engineering*, page 107052, 2019.

R. Mönig, R. R. Keller, and C. A. Volkert. Thermal fatigue testing of thin metal films. *Review of Scientific Instruments*, 75(11):4997–5004, 2004.

A. Molinari. Averaging models for heterogeneous viscoplastic and elastic viscoplastic materials. *J. Engng. Mat. Tech.*, 124:62–70, 2002.

A. Molinari, G.R. Canova, and S. Ahzi. A self consistent approach of the large deformation polycrystal viscoplasticity. *Acta Metall*, 35:2983–2994, 1987.

A. Molinari, S. Ahzi, and R. Kouddane. On the self-consistent modelling of elastic-plastic behavior of polycrystals. *Mech. Mater.*, 26:43–62, 1997.

H. Moulinec and P. Suquet. Numerical method for computing the overall response of nonlinear composites with complex microstructure. *Computational Methods in Applied Mechanics and Engineering*, 157:69–94, 1998.

S. Msolli, M. Martiny, M. Costa Cardoso, L. Pessanha Moreira, S. Mercier, and A. Molinari. Numerical modeling of the deformation of AISI 304L using a tangent additive mori-tanaka homogenization scheme: Application to sheet metal forming. *Journal of Materials Processing Technology*, 235:187 – 205, 2016.

H. Mughrabi. The cyclic hardening and saturation behaviour of copper single crystals. *Materials Science and Engineering*, 33(2):207 – 223, 1978.

N. Ohno and J.-D. Wang. Kinematic hardening rules with critical state of dynamic recovery, part I: formulation and basic features for ratchetting behavior. *International Journal of Plasticity*, 9(3):375 – 390, 1993.

C. Okoro, K. Vanstreels, R. Labie, O. Lühn, B. Vandevelde, B. Verlinden, and D. Vandepitte. Influence of annealing conditions on the mechanical and microstructural behavior of electroplated Cu-TSV. *Journal of Micromechanics and Microengineering*, 20(4):045032, 2010.

J. Pan and J. R. Rice. Rate sensitivity of plastic flow and implications for yield-surface vertices. *International Journal of Solids and Structures*, 19(11):973 – 987, 1983.

P. Ponte Castañeda and P. Suquet. Nonlinear composites. *Adv. Appl. Mech.*, 34:171–302, 1998.

K.V. Rasmussen and O.B. Pedersen. Fatigue of copper polycrystals at low plastic strain amplitudes. *Acta Metallurgica*, 28(11):1467 – 1478, 1980.

D.T Read, Y.W Cheng, and R Geiss. Morphology, microstructure, and mechanical properties of a copper electrodeposit. *Microelectronic Engineering*, 75:63 – 70, 2004.

T. Ritzdorf, L. Graham, S. Jin, C. Mu, and D. Fraser. Self-annealing of electrochemically deposited copper films in advanced interconnect applications. In *Proceedings of the IEEE 1998 International Interconnect Technology Conference (Cat. No. 98EX102)*, pages 166–168. IEEE, 1998.

H. Sabar, M. Berveiller, V. Favier, and S. Berbenni. A new class of micro-macro models for elastic-viscoplastic heterogeneous materials. *Int. J. Solids Structures*, 39:3257–3276, 2002.

A. Salahouelhadj, M. Martiny, S. Mercier, L. Bodin, D. Manteigas, and B. Stephan. Reliability of thermally stressed rigid–flex printed circuit boards for high density interconnect applications. *Microelectronics Reliability*, 54(1):204 – 213, 2014.

M. Sauzay, P. Evrard, A. Steckmeyer, and E. Ferrié. Physically-based modeling of the cyclic macroscopic behaviour of metals. *Procedia Engineering*, 2(1):531 – 540, 2010.

R. Schwaiger, G. Dehm, and O. Kraft. Cyclic deformation of polycrystalline cu films. *Philosophical Magazine*, 83(6):693–710, 2003.

J. Segurado, R. A. Lebensohn, J. LLorca, and C. N. Tomé. Multiscale modeling of plasticity based on embedding the viscoplastic self-consistent formulation in implicit finite elements. *International Journal of Plasticity*, 28 (1):124 – 140, 2012.

F. Siska, S. Forest, P. Gumbsch, and D. Weygand. Finite element simulations of the cyclic elastoplastic behaviour of copper thin films. *Modelling Simul. Mater. Sci. Eng.*, 15:S217–S238, 2007.

L.S. Tóth, A. Molinari, and N. Zouhal. Cyclic plasticity phenomena as predicted by polycrystal plasticity. *Mech. Materials*, 32:99–113, 2000.

L.S. Tóth, S. Biswas, C. Gu, and B. Beausir. Notes on representing grain size distributions obtained by electron backscatter diffraction. *Materials Characterization*, 84:67–71, 2013.

H. Wang, P.D. Wu, C.N. Tomé, and Y. Huang. A finite strain elastic–viscoplastic self-consistent model for polycrystalline materials. *Journal of the Mechanics and Physics of Solids*, 58(4):594 – 612, 2010a.

J. Wang, N. Li, O. Anderoglu, X. Zhang, A. Misra, J.Y. Huang, and J.P. Hirth. Detwinning mechanisms for growth twins in face-centered cubic metals. *Acta Materialia*, 58(6):2262 – 2270, 2010b.

K. Watanabe, Y. Kariya, N. Yajima, K. Obinata, Y. Hiroshima, S. Kikuchi, A. Matsui, and H. Shimizu. Low-cycle fatigue testing and thermal fatigue life prediction of electroplated copper thin film for through hole via. *Microelectronics Reliability*, 82:20 – 27, 2018.

G. J. Weng. A unified, self-consistent theory for the plastic-creep deformation of metals. *J. Appl. Mech.*, 49: 728–734, 1982.

A. Wimmer, A. Leitner, T. Detzel, W. Robl, W. Heinz, R. Pippan, and G. Dehm. Damage evolution during cyclic tension–tension loading of micron-sized cu lines. *Acta Materialia*, 67:297 – 307, 2014.

A. Zaoui and R. Masson. Micromechanics-based modeling of plastic polycrystals: an affine formulation. *Materials Science and Engineering: A*, 285:418–424, 2000.

M. Zecevic and M. Knezevic. An implicit formulation of the elasto-plastic self-consistent polycrystal plasticity model and its implementation in implicit finite elements. *Mechanics of Materials*, 136:103065, 2019.

M. Zecevic and R. A. Lebensohn. New robust self-consistent homogenization schemes of elasto-viscoplastic polycrystals. *International Journal of Solids and Structures*, 202:434 – 453, 2020.

M. Zecevic, I. J. Beyerlein, and M. Knezevic. Coupling elasto-plastic self-consistent crystal plasticity and implicit finite elements: Applications to compression, cyclic tension-compression, and bending to large strains. *International Journal of Plasticity*, 93:187 – 211, 2017.